nature cell biology

Midbody accumulation through evasion of autophagy contributes to cellular reprogramming and tumorigenicity

Tse-Chun Kuo[1,9], Chun-Ting Chen[1,9], Desiree Baron[1], Tamer T. Onder[2,3,4,5], Sabine Loewer[2,3,4,5], Sandra Almeida[6], Cara M. Weismann[1,6], Ping Xu[1], Jean-Marie Houghton[7], Fen-Biao Gao[6], George Q. Daley[2,3,4,5,8] and Stephen Doxsey[1,10]

The midbody is a singular organelle formed between daughter cells during cytokinesis and required for their final separation. Midbodies persist in cells long after division as midbody derivatives (MB^{d}s), but their fate is unclear. Here we show that MB^{d}s are inherited asymmetrically by the daughter cell with the older centrosome. They selectively accumulate in stem cells, induced pluripotent stem cells and potential cancer 'stem cells' *in vivo* and *in vitro*. MB^d loss accompanies stem-cell differentiation, and involves autophagic degradation mediated by binding of the autophagic receptor NBR1 to the midbody protein CEP55. Differentiating cells and normal dividing cells do not accumulate MB^{d}s and possess high autophagic activity. Stem cells and cancer cells accumulate MB^{d}s by evading autophagosome encapsulation and exhibit low autophagic activity. MB^d enrichment enhances reprogramming to induced pluripotent stem cells and increases the *in vitro* tumorigenicity of cancer cells. These results indicate unexpected roles for MB^{d}s in stem cells and cancer 'stem cells'.

Cell division culminates in the separation of two genetically identical daughter cells[1]. During division, cell-fate determinants segregate asymmetrically to stem-cell progeny[2]. The two spindle poles organized by differentially aged centrosomes contribute to this asymmetry[2,3] in that the older centrosome is inherited by the daughter cell that retains the stem-cell fate[4–6].

Abscission completes cell division by severing the intercellular bridge between the two future daughter cells[1,7]. Within the intercellular bridge lies the midbody, a large proteinaceous organelle[7–10] that was previously thought to detach from cells and disintegrate extracellularly as a remnant[7,8]. Recent studies show that post-abscission midbodies or MB^{d}s can be retained by daughter cells, indicating alternative fates for these organelles[9,11,12].

The fate and function of MB^{d}s is unclear. In neural progenitors, MB^{d}s possess the putative stem-cell marker CD133 (also known as prominin-1) and are proposed to participate in intercellular signalling during neural development[13,14]. MB^{d}s can be degraded by autophagy (see below)[12], but the relationship between MB^d loss or retention and the physiological state of cells is unknown.

During autophagy (macroautophagy), double membrane-bound autophagosomes assemble, engulf cytoplasmic material and fuse with lysosomes for degradation[15–18]. Autophagy is required for cellular homeostasis, elimination of defective ubiquitin-tagged proteins and organelles[16–19], clearing of cell-fate determinants and cell remodeling[20–22]. Defects in autophagy contribute to many disorders, including neurodegeneration[23], hepatomegaly[24] and ageing[15,18].

Here we show that MB^{d}s accumulate in stem cells and are lost on differentiation. They are selectively degraded by linking the NBR1 autophagic receptor to the CEP55 midbody protein. MB^{d}s accumulate by evasion of autophagosome encapsulation, asymmetric inheritance and maintenance of low autophagic activity. Reprogramming efficiency and *in vitro* tumorigenicity are increased following experimental elevation of MB^d levels, indicating non-mitotic roles for these organelles in stem and cancer cells.

[1]Program in Molecular Medicine, University of Massachusetts Medical School, Worcester, Massachusetts 01605, USA. [2]Stem Cell Program, Children's Hospital Boston, Boston, Massachusetts 02115, USA. [3]Stem Cell Transplantation Program, Division of Pediatric Hematology and Oncology, Manton Center for Orphan Disease Research, Children's Hospital Boston and Dana Farber Cancer Institute, Boston, Massachusetts 02115, USA. [4]Department of Biological Chemistry and Molecular Pharmacology, Harvard Medical School, Boston, Massachusetts 02115, USA. [5]Harvard Stem Cell Institute, Cambridge, Massachusetts 02138, USA. [6]Departments of Neurology, University of Massachusetts Medical School, Worcester, Massachusetts 01605, USA. [7]Department of Pathology, University of Massachusetts Medical School, Worcester, Massachusetts 01605, USA. [8]Howard Hughes Medical Institute, Chevy Chase, Maryland 20815, USA. [9]These authors contributed equally to this work. [10]Correspondence should be addressed to S.D. (e-mail: stephen.doxsey@umassmed.edu)

Received 23 August 2010; accepted 3 August 2011; published online 11 September 2011; corrected online 15 November 2011; DOI: 10.1038/ncb2332

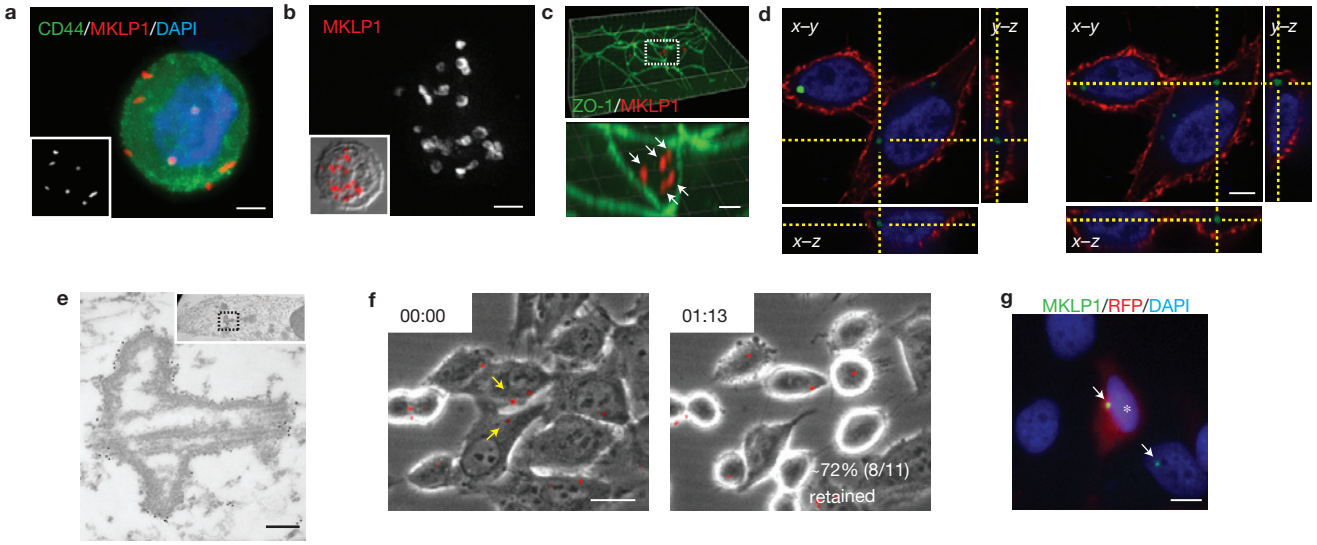

Figure 1 MB^{d}s accumulate within cells. (**a**,**b**) Multiple MB^{d}s associate with a PC3 cell (**a**) and a B-lymphoblast (**b**). Insets: MB^d labelling (**a**) and merged differential interference contrast microscopy image with MB^d labelling to show cell boundaries (**b**). MKLP1, MB^d marker (**a**,**b**; red); CD44, membrane (**a**; green); DAPI, DNA (**a**; blue). Scale bar, 5 μm (**a**) and 2 μm (**b**). (**c**,**d**) Three-dimensional reconstructions of polarized cells in a monolayer (**c**) and a HeLa cell (**d**) show intracellular MB^{d}s. (**c**) ZO-1, tight junction; MKLP1, MB^{d}s. Scale bar, 2 μm. Enlargement (bottom panel) of the box in the top panel shows five MB^{d}s (arrows). (**d**) Wheat-germ agglutinin, plasma membrane (red); MKLP1–GFP, MB^{d}s (green); DAPI, DNA (blue). Scale bar, 5 μm. (**e**) Electron micrograph of an MB^d in a permeabilized MCF-7 cell showing immungold labelling with MKLP1 antibodies. Inset, lower magnification of the MB^d (boxed) in the cell; nucleus, right. Scale bar, 200 nm. (**f**) Time-lapse images during extracellular trypsin treatment of HeLa cells show retention of most MB^{d}s (MKLP1–GFP, red). Two MB^{d}s (yellow arrows) are lost on treatment, indicating digestion and/or dissociation. Time (h:min) post trypsin. Scale bar, 5 μm. (**g**) Two-day co-cultures of HeLa cells expressing either MKLP1–GFP (MB^d marker) or cytosolic RFP. Green MB^{d}s (arrows) associated with red cells (asterisk) indicate post-mitotic transfer of MB^{d}s between cells. Scale bar, 10 μm.

RESULTS

Post-mitotic midbodies accumulate within cells

Multiple MB^{d}s (up to 20) were observed in subpopulations of cells by immunofluorescence, but their precise location was unclear (Fig. 1a,b). Three-dimensional reconstruction of immunofluorescent images revealed multiple MB^{d}s inside polarized and non-polarized cells (Fig. 1c,d). Immuno-electron microscopy confirmed this localization and revealed ultrastructural features characteristic of MB^{d}s (refs 8,14; Fig. 1e). About 70% of cell-associated MB^{d}s were trypsin resistant, indicating that they were intracellular (Fig. 1f). This intracellular localization of MB^{d}s indicated that they might accumulate in cells through successive divisions (see below).

MB^{d}s were also released from cells. In two-day co-cultures of HeLa cells stably expressing either monomeric RFP (red fluorescent protein, cytoplasmic marker) or green fluorescent protein (GFP)-tagged MKLP1 (midbody marker), about 7% of MKLP1–GFP$^+$MB^{d}s associated with RFP$^+$ cells (Fig. 1g). Such free MB^{d}s were also generated by other cell types (for example adult human fibroblasts, HeLa; 1–10%). These observations resolve the conflict of previous studies indicating that MB^{d}s are either retained and degraded[9,11,12] or released as remnants after abscission[8]. We show that MB^{d}s accumulate in some cells (Fig. 1a–d) but not others, and it is this cell-type-specific difference in MB^d accumulation that is the focus of this study.

MB^{d}s are inherited by the cell with the older centrosome

Multiple MB^{d}s often clustered around the centrosome or spindle pole (ref. 9 and data not shown), reminiscent of MB^d-sized aggresomes, which segregate to one daughter cell under control of centrosomes[25,26]. Moreover, centrosome-age-dependent differences in signalling were observed late in cytokinesis[27]. These centrosome-age-related differences led us to examine the relationship between centrosomes and MB^d inheritance.

In G1, the centrosome contains one mother centriole and one daughter centriole[3]. After centriole duplication, three generations of centrioles are present: an older mother, a younger mother and two new daughters[3,27]. The centrosome with the older mother centriole is termed the older centrosome[4,5]. GFP-tagged centrin-1 (CETN1–GFP; ref. 28) expressed in mitotic HeLa cells was brightest at one of the four centrioles (92.2% of cells, $n = 116$; Fig. 2a) and turned over very slowly (fluorescence recovery after photobleaching $t_{1/2} \sim 4$ h and ref. 5). The brightest centriole remained so from metaphase to late cytokinesis (91.3% of cells, $n = 46$; Supplementary Fig. S1a), indicating that this was the older mother centriole. This was confirmed by staining with the older-centrosome marker hCenexin1 (ref. 27; ~90% of HeLa and MCF-7 cells, $n = 143$ and $n = 347$, respectively; Fig. 2b). Several other centriole antigens also showed intrinsic age-related differences in labelling (Supplementary Fig. S1b).

Using CETN1–GFP to identify the older mother centriole, bright-field imaging to follow midbody dynamics in living cells and immunofluorescence to confirm MB^d inheritance, we determined that MB^{d}s were preferentially inherited by the cell with the older centrosome. This was observed in pluripotent human embryonic stem cells (hESCs; 83.3% of H9, $n = 18$; Fig. 2d), immortalized somatic cells (91.3% of hRPE-1, $n = 23$) and cancer cells (84.6% of U2OS, $n = 13$; 75.0% of HeLa, $n = 24$; Fig. 2c). We conclude that most inherited MB^{d}s are asymmetrically transferred to the daughter cell with the older centrosome in several cell types.

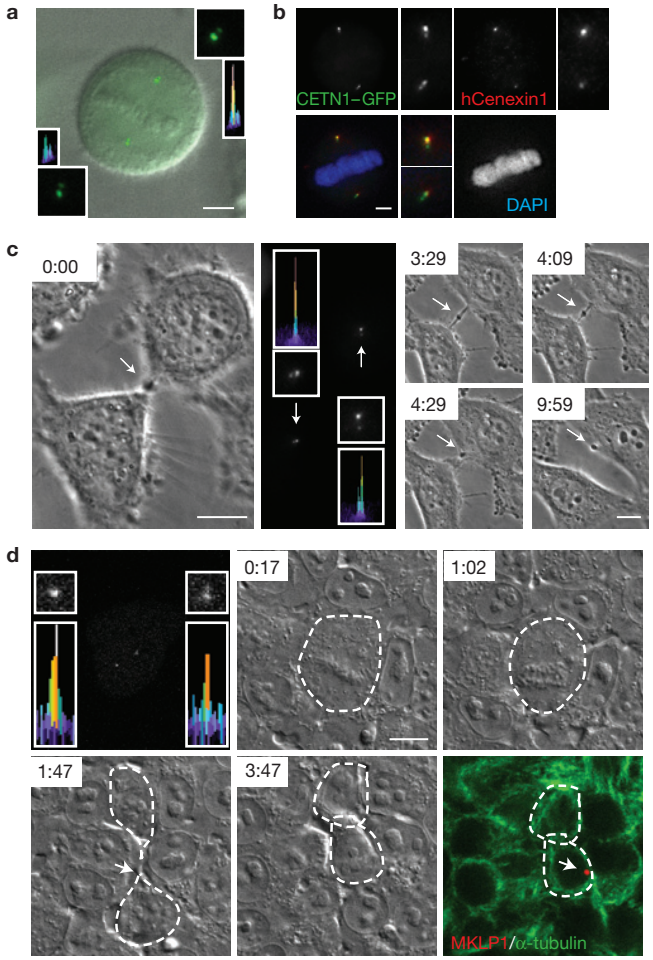

Figure 2 MB^{d}s are preferentially inherited by the cell with the older centrosome. (**a**) The CETN1–GFP signal is brighter in the upper centrosome/spindle pole of a mitotic spindle. The merged differential interference contrast microscopy image with CETN1–GFP labelling at two centrosomes shows a metaphase chromosome. Insets: enlargements and semi-quantitative integrated intensity profiles of centrioles. Scale bar, 5 μm. (**b**) The brighter CETN1–GFP signal represents the older centrosome, as it co-stains more intensely for hCenexin1 and remains more intense throughout cell division (Supplementary Fig. S1a). Scale bar, 5 μm. Lower left, merge. (**c**,**d**) Time-lapse images show that the mitotic midbody is preferentially inherited by the daughter cell with the older centrosome in HeLa cells (**c**) and hESCs (**d**). Cells were imaged at the indicated times (h:min) from telophase by phase-contrast microscopy (**c**) and from metaphase by differential interference contrast microscopy (**d**). Middle panel of (**c**) and upper left panel of (**d**): CETN1–GFP at centrosomes; enlargements and integrated intensity profiles show that the daughter cell with the older centrosome (**c**, upper; **d**, lower) inherits the MB^d (lower right images in **c**,**d**). Mitotic midbody and MB^{d}s (**c**,**d**; arrows). MKLP1, MB^d marker (red); α-tubulin, mitotic midbody and cell-boundary marker (green); DAPI, DNA (blue). Scale bars, 10 μm (**c**,**d**).

MB^{d}s accumulate in stem cells *in vivo*

Other studies have shown that the older centrosome is asymmetrically inherited by the stem cell during asymmetric divisions in the *Drosophila* male germline[4] and the mouse neocortex[5]. The association of the older centrosome with both MB^{d}s and stem-cell divisions led us to ask whether MB^{d}s were found in stem-cell niches. To address this, we determined the localization of MB^{d}s in human and mouse tissues. In seminiferous tubules of testes, MB^{d}s were confined to the basal compartment, the site of germline stem cells and their

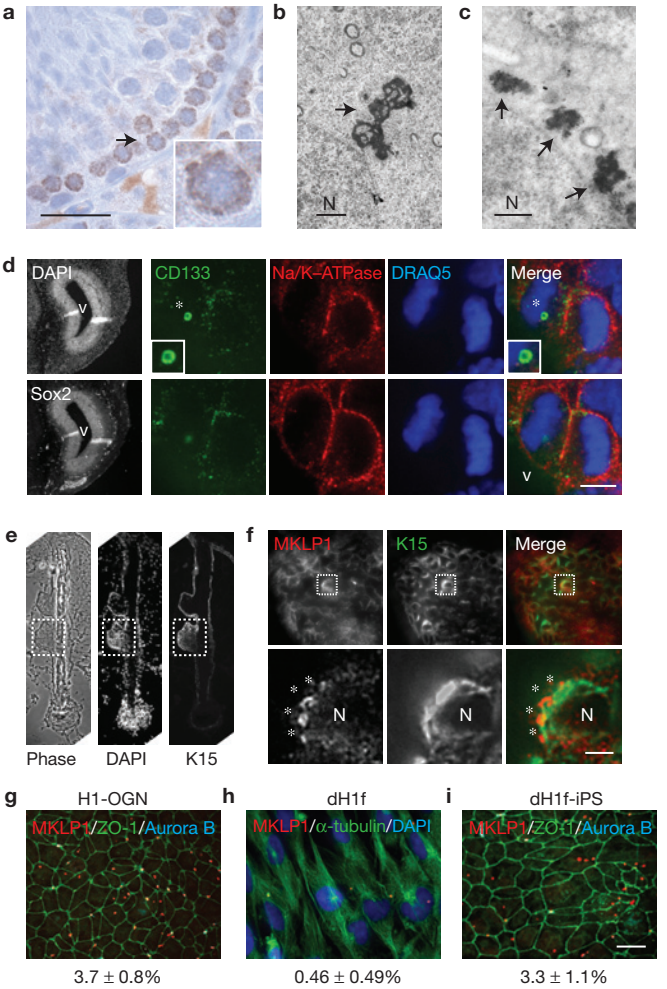

Figure 3 MB^{d}s accumulate in stem cells *in vivo* and *in vitro*. (**a**) A histological section through mouse seminiferous tubules labelled for MKLP1 shows several MKLP1$^+$ puncta in cells of the basal layer where stem cells reside. Scale bar, 20 μm. Inset: Enlargement of the cell marked by the arrow. (**b**,**c**) Electron micrographs of mitotic midbody (**b**, arrow) and multiple midbody-like structures in interphase cells with similar shapes and sizes in a juxtanuclear position (**c**, arrows) in basal cells of mouse seminiferous tubules. N, nucleus. Scale bars, 1 μm. (**d**) Representative planes of a neural progenitor cell in the ventricular zone (Sox2$^+$, bottom left panel) of an E13.5 mouse brain show that an intracellular MB^d (asterisk) is associated with the ventricle-facing daughter in the asymmetrically dividing cell (top row). The bottom row emphasizes the position of paired chromosomes in a dividing anaphase cell. CD133, midbody/MB^d marker (green); Na/K-ATPase, cell-border marker (red); DRAQ5, DNA (blue); DAPI, DNA. v, ventricle. Scale bar, 5 μm. Note that abscission occurs apically in these cells. (**e**) A histological section through a hair follicle (left, phase-contrast microscopy) stained for the stem-cell marker keratin 15 (K15) to identify the bulge region (dotted box), the stem-cell niche. DNA stain (DAPI) and the phase-contrast microscopy image show full follicle architecture. (**f**) Upper panels show MB^d-accumulating cells in the bulge region (boxed) co-labelled with K15 and MKLP1. Enlargements (lower panels) of the boxed region highlight a cell with four MB^{d}s (asterisks). N, nucleus. Scale bar, 5 μm. (**g**–**i**) Quantitative analysis and representative images show a decrease in MB^d-accumulating cells on the differentiation of pluripotent stem cells (**g**) to fibroblast-like cells (**h**), and an increase in MB^d-accumulating cells after reprogramming differentiated cells (**h**) to induced pluripotent stem cells (**i**). Numbers refer to mean ± s.d., $n = 3$. MKLP1, MB^{d}s; ZO-1, tight junctions; α-tubulin, microtubules; Aurora B, midbodies. Scale bar, 10 μm.

mitotic progeny (both capable of self-renewal[29,30]) (Fig. 3a, up to eight puncta/cell, 5 μm section). Electron microscopy also revealed

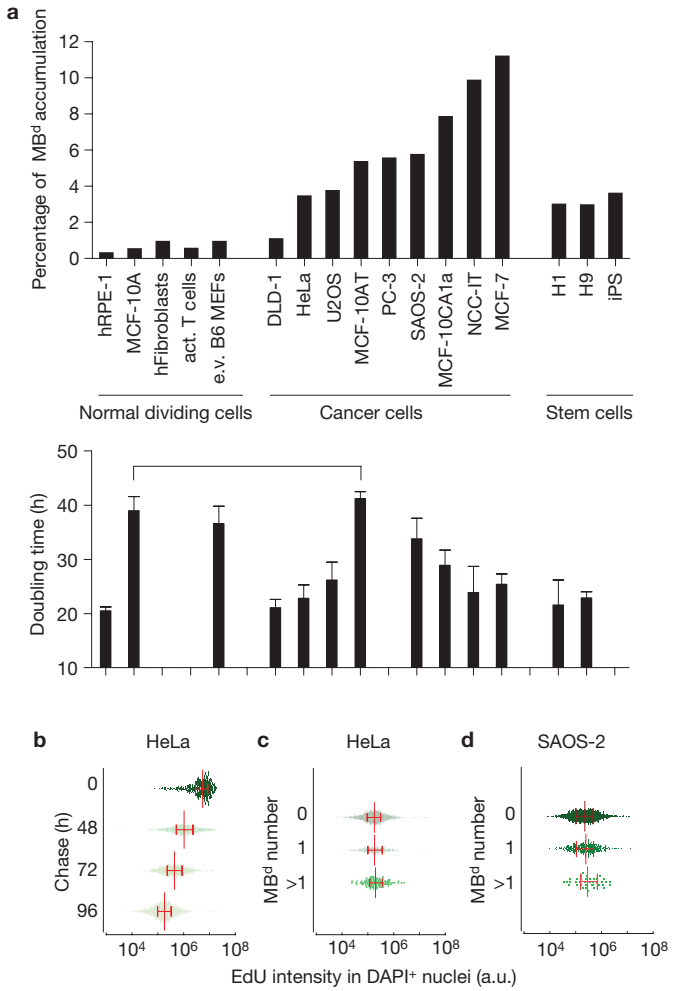

Figure 4 MB^d accumulation is high in stem cells and subpopulations of cancer cells and does not correlate with cell doubling time. (**a**) Above: percentages of cells that accumulate MB^{d}s (>1) in a range of different cell types, as indicated. Below: doubling times of representative cell lines aligned with MB^d-accumulation data. Data are presented as mean±s.d.; cell lines are examined in triplicate (MCF-10A, DLD-1, MCF-10AT, MCF-7, H1 and H9) or quadruplicate (e.v. B6 MEFs, HeLa, SAOS-2 and MCF-10CA1a), except hRPE-1 ($n=6$), U2OS ($n=7$) and NCC-IT ($n=8$). Horizontal line, cell lines with different MB^d accumulation potentials (14-fold) but similar doubling times. (**b**) Cells pulse-chased with EdU show a decrease in EdU intensity (*x* axis) over time (*y* axis), reflecting dilution of dye after cell divisions. (**c**,**d**) After a 96 h chase period, EdU levels were compared between cells with MB^d numbers of >1, 1 and 0 (*y* axis) in HeLa (**c**) and SAOS-2 cells (**d**). In both cases, no significant differences were noted (**c**, $P=0.2101$; **d**, $P=0.5609$, one-way analysis of variance, with at least 800 cells analysed for each experiment, $n=3$), indicating similar cycling rates among different subpopulations of cells. (**b**–**d**) Each graph is a representative experiment. Cells analysed are shown by green points, the medians are depicted by vertical red lines, and horizontal red lines with ticks illustrate the interquartile range.

multiple cytoplasmic structures with features characteristic of MB^{d}s within these cells (Fig. 3b,c).

In the ventricular zone (Sox2$^+$; ref. 31) of embryonic mouse brains, CD133-labelled MB^{d}s were associated with neural progenitors[13,14] (Fig. 3d and Supplementary Fig. S2). During asymmetric divisions, intracellular MB^{d}s were usually found in ventricle-facing daughter cells (progenitors; 75%, $n=8$) and not in daughters with presumed committed fates[5]. MB^{d}s in the human hair follicle were also confined to a subpopulation of cells in the stem-cell niche, the bulge[32], indicating distinct properties of this subpopulation (Fig. 3e,f). MB^{d}s were also enriched in β1 integrin$^+$ (ref. 33) mouse skeletal muscle progenitors (SMPs; fourfold) over non-SMP cells. These observations indicated that MB^{d}s were selectively retained and accumulated during successive stem-cell divisions *in vivo*.

MB^{d}s accumulate in stem cells *in vitro*

To rigorously test the idea that MB^{d}s are selectively inherited by stem cells, we examined MB^d fate during stem-cell differentiation and somatic-cell reprogramming. MB^d 'accumulation' was assessed by counting cells with more than one MB^d, as all cells can transiently acquire one MB^d after abscission (see below). MB^d accumulation decreased ~8-fold on differentiation of hESCs (H1-OGN) to fibroblast-like cells (dH1f; Fig. 3g,h). Differentiation was judged by loss of embryonic stem-cell markers (Oct4, SOX2, KLF4, NANOG) and gain of the CD13 differentiation marker[34,35]. In contrast, MB^d accumulation increased ~7-fold after reprogramming dH1f cells to induced pluripotent stem cells (iPSCs; refs 34,36; dH1f-iPS; Fig. 3h,i). We conclude that MB^d accumulation *in vitro* reflects that observed *in vivo*, and can be manipulated by altering the potency status of cells.

MB^d accumulation is enhanced in tumour-derived cells

We next examined differences in MB^d accumulation among cell lines derived from stem cells, normal dividing cells and cancer cells (Fig. 4a). MB^d accumulation was low in primary and telomerase-immortalized normal cells and significantly higher in hESCs and iPSCs (~7-fold on average; Fig. 4a). Most cancer cells exhibited even higher levels of MB^d accumulation. For example, MB^d accumulation in tumorigenic MCF-10AT and MCF-10CA1a cells was much higher than in the normal MCF-10A parental line. The common ability of stem cells and cancer cells to accumulate MB^{d}s, express stem-cell markers[37] and possess stem-cell properties[38,39] indicates a relationship between MB^d accumulation, tumorigenicity and cancer 'initiating' or 'stem' cells defined by the cancer 'stem cell' (CSC) theory[40].

MB^d accumulation does not correlate with cell proliferation rate

A simple explanation for cell-type-specific differences in MB^d accumulation is variability in proliferation rates. Slower division rates could provide more time for MB^d degradation, as recently proposed[12]. However, we observed no correlation between population doubling time and MB^d accumulation (Fig. 4a). It was still possible that MB^d-accumulating cells cycled faster than the bulk population. However, a cohort of cells pulse-labelled with 5-ethynyl-2′-deoxyuridine (EdU; ref. 41) showed a proportional decrease in EdU intensity, reflecting dilution of dye after successive divisions (Fig. 4b) and indicating that MB^d-accumulating and non-accumulating subpopulations had similar cycling rates (Fig. 4c,d).

MB^d-accumulating cells evade membrane encapsulation of MB^{d}s

We next asked if MB^{d}s occupied different sites within MB^d-rich and MB^d-poor cells. To test this, we used the fluorescence protease protection (FPP) assay[42] to monitor degradation of MB^{d}s following plasma-membrane permeabilization and protease addition (Fig. 5a).

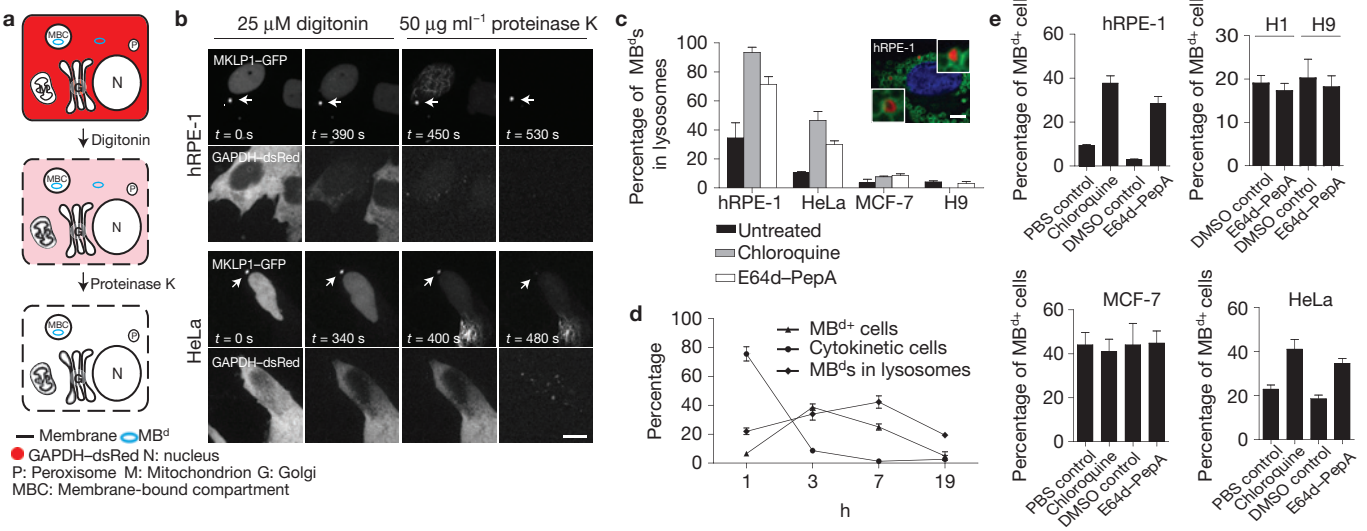

Figure 5 MB^{d}s in stem and cancer cells evade membrane encapsulation and lysosomal degradation. (**a**) Depiction of FPP assay. Digitonin selectively permeabilizes the plasma membrane but not internal membranes. Proteinase K degrades cytoplasmic components but membranous compartments remain intact. Under these conditions, MKLP1–GFP-labelled MB^{d}s (blue ellipse) in the cytoplasm will be degraded whereas those inside membrane-bound compartments will not. (**b**) MB^{d}s in MB^d-poor hRPE-1 cells are largely protected (~90% in membranous compartments, 10 cells analysed), whereas most MB^{d}s in HeLa cells are not (~27%, 11 cells analysed), and are thus degraded in cytoplasm. Scale bar, 5 μm. (**c**) Presence of MB^{d}s in lysosomes on chloroquine or E64d–pepstatin A (E64d–PepA) inhibition in hRPE-1 and HeLa cells, but not in MCF-7 and H9 hESCs. Chloroquine treatment of H9 hESCs is not included as it caused differentiation and cell death. A representative image of hRPE-1 cells inhibited by chloroquine is shown, depicting two MB^{d}s inside lysosomes. MKLP1 and LAMP2 are used as MB^d (red) and lysosome (green) markers, respectively. DAPI, DNA (blue). $n = 100$ MB^{d}s per treatment in each of the biological triplicates. Scale bar, 5 μm. (**d**) Percentage of MB^{d+} cells (MB^d levels), percentage of MB^{d}s within lysosomes and percentage of cells exiting cytokinesis following synchronization. MKLP1 and LAMP2 are used as markers as in **c**. Note that MB^{d}s are transferred into only one of the two nascent daughter cells after abscission (Fig. 2d), so a 50% maximum will be expected for MB^{d+} cells. The peak of MB^{d}s transferred to cells is 3 h after plating followed by a peak of MB^{d}s entering lysosomes at 7 h. (**e**) Both chloroquine and E64d–PepA treatments increase the percentage of MB^{d+} cells in hRPE-1 cells and HeLa cells (chloroquine, $P = 0.0021$ and $P = 0.0187$, respectively; E64d–PepA, $P = 0.0022$ and $P = 0.0043$, respectively; $n = 3$ for all experiments). In contrast, lysosomal inhibition has no detectable effect on hESCs (H1, H9) or MCF-7 cancer cells. DMSO, dimethylsulphoxide. Data are presented as mean ± s.d. (**c**–**e**), except mean ± s.e.m. in hESCs (**e**).

Under these conditions, MKLP1–GFP$^+$ MB^{d}s were degraded in MB^d-rich HeLa cells but not in MB^d-poor hRPE-1 cells, indicating that MB^d-poor cells sequestered MB^{d}s in membrane-bound compartments whereas MB^d-rich cells accumulated them in the cytoplasm (Fig. 5b). Importantly, the integrity of intracellular organelles was maintained during the course of these experiments (Supplementary Fig. S3).

Stem cells and cancer cells evade lysosomal degradation of MB^{d}s

The protease resistance of MB^{d}s and low MB^d accumulation in MB^d-poor hRPE-1 cells (Figs 4a and 5b) indicated that MB^{d}s were delivered to a membrane-bound compartment for degradation, such as the lysosome. Indeed, MB^{d}s were often found within LAMP2-labelled (ref. 43) lysosomes in MB^d-poor cells (Fig. 5c). To test this further, we examined the fate of newly formed MB^{d}s in synchronous populations of MB^d-poor cells (Fig. 5d). Three hours after release from mitosis, the percentage of MB^{d+} cells (MB^d levels) peaked at ~40% (50% being the maximum, because half the cells were 'born' without an MB^d). This was followed by a peak in MB^d localization to lysosomes (~42% at 7 h; Fig. 5d) and then a decrease of MB^{d}s to baseline levels (16–19 h; Fig. 5d). These data and the FPP data indicated that MB^{d}s in hRPE-1 cells entered the cytoplasm, moved into lysosomes and were degraded before the next cell cycle (Fig. 5b,d).

If lysosomes are involved in MB^d degradation, lysosomal inhibition should increase MB^d levels. Indeed, when lysosomal activity was inhibited in MB^d-poor hRPE-1 cells with either chloroquine or E64d–PepA protease inhibitors[44], MB^d levels (Fig. 5e) and the percentage of MB^{d}s found within lysosomes (Fig. 5c) were elevated. In contrast, MB^d levels and the percentage of MB^{d}s in lysosomes in MB^d-rich cells (hESC, MCF-7; Fig. 5c,e) were largely unaffected by lysosomal inhibition (see Supplementary Fig. S4a). The modest increase in MB^{d+} HeLa cells (Fig. 5e) was consistent with their modest MB^d-accumulating ability (Fig. 4a). We conclude that lysosomal degradation prevents MB^d accumulation in MB^d-poor cells, but does not play a major role in MB^d-rich cells (for example stem cells, CSCs), thus enabling MB^{d}s to accumulate.

Autophagic degradation controls intracellular MB^d levels

To determine how MB^{d}s were directed to lysosomes, we explored pathways leading to lysosomal degradation. Reported autophagy levels in MCF-7 and DLD-1 cells[45,46] indicated a relationship between autophagy and MB^d fate. Low autophagy levels in MCF-7 cells resulting from a deficiency in the autophagy gene, *BECN1* (also known as *ATG6*; ref. 45), are consistent with high MB^d accumulation (~26-fold over normal cells; Fig. 4a). High autophagy levels in DLD-1 cells[46] are consistent with low MB^d accumulation (only ~1.8-fold over normal cells; Fig. 4a). In agreement with this trend was the presence of MB^{d}s in autophagosomes of MB^d-poor cells (Fig. 6a).

Experimental reduction of autophagy activity using mouse embryonic fibroblasts (MEFs) from *Atg5*-deleted mice[19] or by short

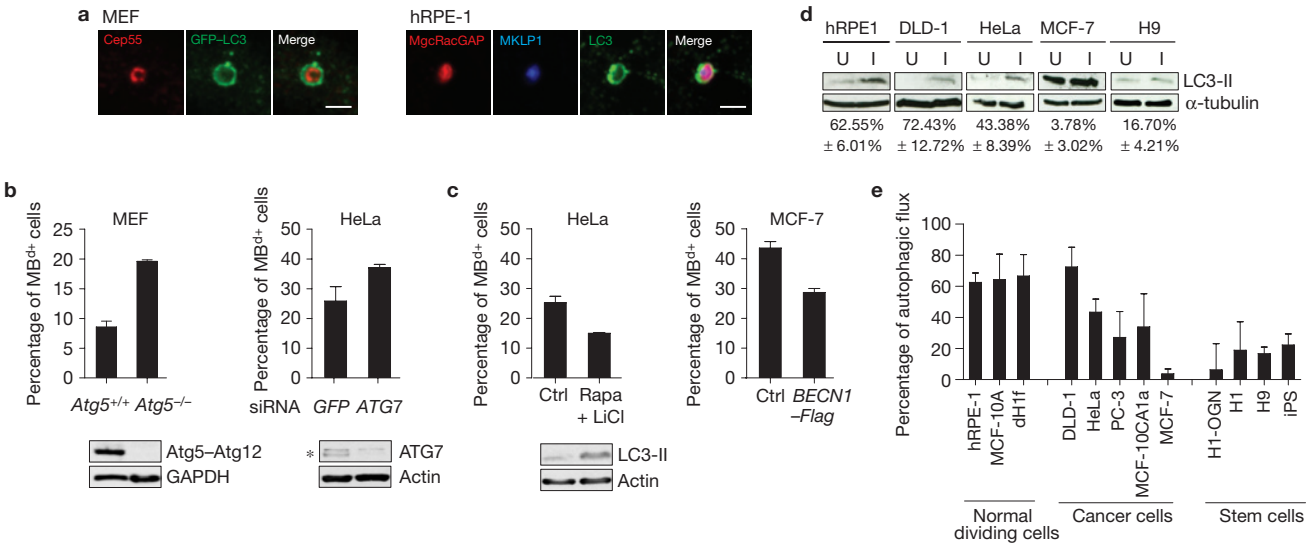

Figure 6 Autophagy controls intracellular MB^{d} levels. (**a**) Single-plane confocal microscopy images of MB^{d}s within LC3-positive autophagosomes in MEFs expressing GFP–LC3 (left) and in hRPE-1 cells stained for endogenous LC3 (right). MB^{d} markers: Cep55, MKLP1 or MgcRacGAP. Autophagosomes: GFP–LC3 or LC3. Note that MKLP1 (blue) and MgcRacGAP (red) are co-localized (magenta) in the autophagosome (green), indicating that MB^{d}s are sorted into autophagosomes. Scale bars, 2 μm. (**b**) Decreasing autophagy levels by deletion of the *Atg5* gene (left) or depletion of ATG7 by siRNA (right) significantly increases the percentage of MB^{d+} cells ($P = 0.0019$ and $P = 0.021$, respectively, $n = 3$). Immunoblots confirm loss of the Atg5–Atg12 conjugation in mutant cells and depletion of ATG7 (asterisk). GAPDH, glyceraldehyde 3-phosphate dehydrogenase. (**c**) Rapamycin (Rapa) and LiCl co-treatment induces autophagy and decreases the percentage of MB^{d+} cells (left, HeLa; $P = 0.0056$, $n = 3$). Immunoblots showing increased LC3-II levels confirm autophagy induction. Induction of autophagy by overexpression of Flag-tagged BECN1 reduces the percentage of MB^{d+} cells (right, MCF-7; $P = 0.0008$, $n = 4$). Ctrl, control. (**d**) Representative immunoblots showing high autophagy levels in normal cells and low levels in stem cells and cancer cells. Autophagic flux (autophagic activity) was measured by changes in the levels of LC3-II, in the presence or absence of lysosomal inhibitors E64d–PepA. U, uninhibited. I, inhibited. Below, the average of the percentage change in LC3-II levels after lysosomal inhibition from three experiments. α-tubulin, loading control. (**e**) Quantification of autophagic flux from three experiments in different cell lines. Normal dividing cells (MB^{d} poor) typically have high autophagic flux, whereas stem and cancer cells (MB^{d} rich) have low autophagic flux. The data are presented as mean ± s.d. (**b**–**e**). Uncropped images of blots are shown in Supplementary Fig. S6.

interfering RNA (siRNA)-mediated depletion of ATG7 increased MB^{d} levels (Fig. 6b). Induction of autophagy by rapamycin and lithium chloride treatment[47,48] in HeLa cells or by exogenous BECN1 expression in MCF-7 cells decreased MB^{d} levels (Fig. 6c). These results demonstrate the role of autophagy in regulating MB^{d} levels in different cell types, and indicate an inverse relationship between autophagic activity and MB^{d} accumulation. This inverse relationship was revealed in 12 cell lines by microtubule-associated protein light chain 3-II (LC3-II) (refs 44,49) or p62-based (refs 44,50,51) measurements of autophagic activity (Fig. 6d,e and Supplementary Fig. S4b). We conclude that MB^{d} levels are, in part, modulated by cell type/lineage-specific autophagy (Figs 3g–i, 4a, 6d,e).

NBR1 is an autophagic receptor for MB^{d}-specific degradation

To test whether MB^{d} degradation involves non-specific or receptor-mediated autophagy pathways[15], we investigated the mammalian autophagic receptors p62 (refs 50–52) and NBR1 (refs 53,54). p62 is implicated in MB^{d} clearance[12], whereas NBR1 is untested. NBR1 and p62 localized to mitotic midbodies and MB^{d}s (Fig. 7a, top, data not shown, and ref. 12), indicating that MB^{d} degradation involves receptor-mediated autophagy. *NBR1* silencing in HeLa cells increased MB^{d} levels to *ATG7*-silencing levels (Figs 6b and 7b), indicating that NBR1 is probably a major autophagic receptor for MB^{d} degradation. In contrast, *p62* deletion[51] or siRNA-mediated p62 depletion had no detectable effect on MB^{d} levels (Fig. 7b,c) or NBR1 recruitment to MB^{d}s (Fig. 7a, bottom).

So far, no MB^{d} targets for autophagic degradation have been identified. Candidate-based screening revealed that endogenous NBR1 co-immunoprecipitated with the midbody protein CEP55 in hRPE-1 cells (Fig. 7d). CEP55 overexpression increased MB^{d} levels (Fig. 7e) and the level of NBR1-negative MB^{d}s (Fig. 7f), presumably through NBR1 sequestration in the cytoplasm (Fig. 7g). This indicated a role for CEP55 in NBR1-mediated MB^{d} degradation. We propose that the CEP55–NBR1 interaction couples MB^{d}s to the autophagic machinery to control MB^{d} fate.

Cells enriched in MB^{d}s exhibit increased reprogramming efficiency

We next examined the functional consequences of manipulating MB^{d} levels. We first tested the role of MB^{d}s during reprogramming[34,35,55] in cells stably expressing NBR1-specific short hairpin RNAs (shRNAs) to increase MB^{d} levels over controls (non-targeting shRNA, shNT). MB^{d} levels increased ~1.8-fold in dH1f cells, ~1.5-fold in IMR90 (ref. 55) embryonic fibroblasts and ~1.9-fold in hFib2 (ref. 34) adult fibroblasts. Under these conditions, iPSC colony formation increased significantly in all three cell types depleted of NBR1: dH1f cells (up to 8.7-fold, average 3.1 ± 0.5-fold), IMR90 cells (up to 4.2-fold, average 3.4 ± 0.8-fold; Fig. 8a,b and Supplementary Table S1) and adult hFib2 cells (up to 2.5-fold, average 1.7 ± 0.5-fold). Similar results were obtained with different batches of viruses, different combinations of reprogramming factors and different viral delivery systems (see Methods). Importantly, increased reprogramming

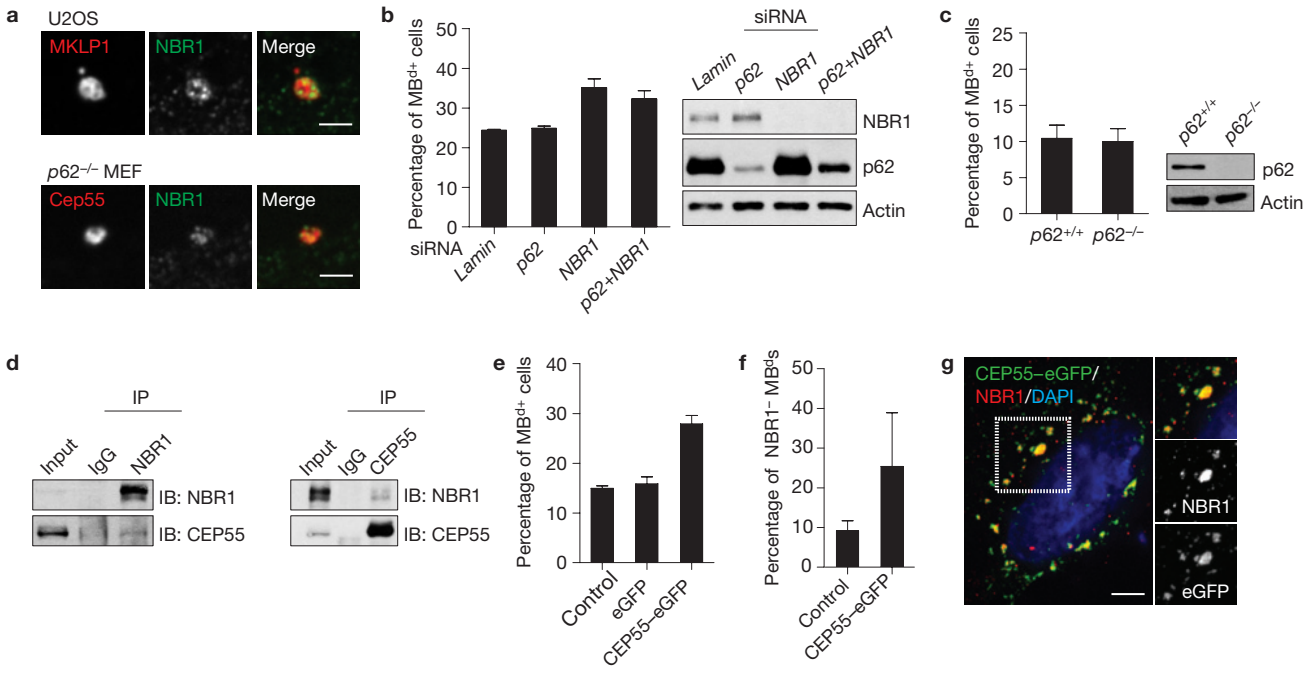

Figure 7 NBR1 is a receptor for targeting MB^{d}s to the autophagy pathway. (**a**) Single-plane confocal microscopy images showing co-localization of the MB^{d}s and the autophagic receptor NBR1 in U2OS cells and *p62*-deleted MEFs. MB^{d} markers: MKLP1 or Cep55. Scale bar, 2 μm. (**b**) The percentage of MB^{d+} cells is significantly increased following the depletion of NBR1 ($P = 0.022$, $n = 3$), but not another autophagic receptor, p62. Co-depletion of NBR1 and p62 does not further increase MB^{d} levels over NBR1 depletion alone. (**c**) Deletion of the *p62* gene does not affect the percentage of MB^{d+} cells. For **b** and **c**, immunoblots verify protein loss. (**d**) Co-immunoprecipitation (IP) reveals that CEP55 and NBR1 form a complex. Precipitated proteins and 5% of the input material (Input) were analysed by immunoblotting (IB) with antibodies against NBR1 or CEP55. (**e**–**g**) Overexpression of CEP55–eGFP (enhanced green fluorescent protein) increases the percentage of MB^{d+} cells (**e**; $P = 0.0007$, $n = 3$) and the percentage of NBR1-negative MB^{d}s (**f**; $P = 0.0568$, $n = 3$), presumably by sequestering NBR1 (red) away from MB^{d}s in cells expressing CEP55–eGFP (green) as shown in **g**, and consequently preventing MB^{d} degradation. The dotted box in **g** is enlarged (top right panel), and the labelling of NBR1 and CEP55–eGFP (middle and bottom right panels) are also presented. DAPI, DNA (blue). Scale bar, 5 μm. The data are presented as mean ± s.d. (**b**,**c**,**e**,**f**). Uncropped images of blots are shown in Supplementary Fig. S6.

following NBR1 depletion occurred without significant changes in global autophagic activity (dH1f; Fig. 8c) or cell proliferation rate (*NBR1* shRNA, 27.3 ± 2.5 h; shNT, 26.8 ± 4.5 h; $n = 6$), indicating that NBR1 is selective for MB^{d} degradation.

Cancer cells enriched in MB^{d}s exhibit increased *in vitro* tumorigenicity

Because MB^{d}s selectively accumulate in stem-cell niches, hESCs and iPSCs, we reasoned that they may also accumulate in CSCs. On the basis of Hoechst 33343 extrusion, the side population of MCF-7 cells[56] was isolated. These putative CSCs showed a sevenfold increase in MB^{d+} cells over the non-side-population (MP; Fig. 8d).

To directly address the role of MB^{d}s in cancer cells, MKLP1–GFP-expressing HeLa populations with high or low percentages of MB^{d+} cells were isolated by FACS, and tested for anchorage-independent growth. Increased colony formation was observed in the 'MB^{d}-high' versus the 'MB^{d}-low' population, and colony formation increased with increasing MB^{d} levels (up to fourfold; Fig. 8e). An increase in colony formation was also observed in MB^{d}-enriched HeLa cells (Fig. 8f, left) and mouse hepatocarcinoma cells (134-4; Fig. 8f, right) following *NBR1* silencing. Results of all three strategies indicate that MB^{d}s in cancer cell subpopulations may contribute to their tumorigenic potential.

DISCUSSION

We have identified new roles for MB^{d}s outside their canonical function in cytokinesis. This work provides evidence for MB^{d} accumulation in stem cells, hESCs and iPSCs *in vivo* and *in vitro*, and for marked MB^{d} reduction in differentiating progeny of stem cells. MB^{d}s seem to function in maintaining or enhancing the pluripotency of stem cells and the tumorigenicity of cancer cells.

Our findings indicate that the MB^{d} loss that accompanies stem-cell differentiation is mediated by autophagic degradation, resulting in selective elimination of MB^{d}s in differentiated cells but retention in germ or stem cells. This process is intriguingly similar to clearance of P granule components in committed somatic cells of *Caenorhabditis elegans*, which is also mediated by autophagy[57]. Moreover, P granules contain molecules required for cell-fate specification[58], and MB^{d}s contain stem-cell markers[13,14] and enhance cell-fate conversion (present study). It is thus tempting to propose that MB^{d}s may serve as scaffolds for organizing cell-fate determinants. Equally intriguing is the observation that essentially all cancer cells examined contain MB^{d}-accumulating subpopulations, making this a common intrinsic property of both stem cells and cancer cells. The observation that MB^{d}-enriched cancer subpopulations exhibit enhanced *in vitro* tumorigenicity is consistent with the CSC model for potentiation of tumorigenicity[37–40].

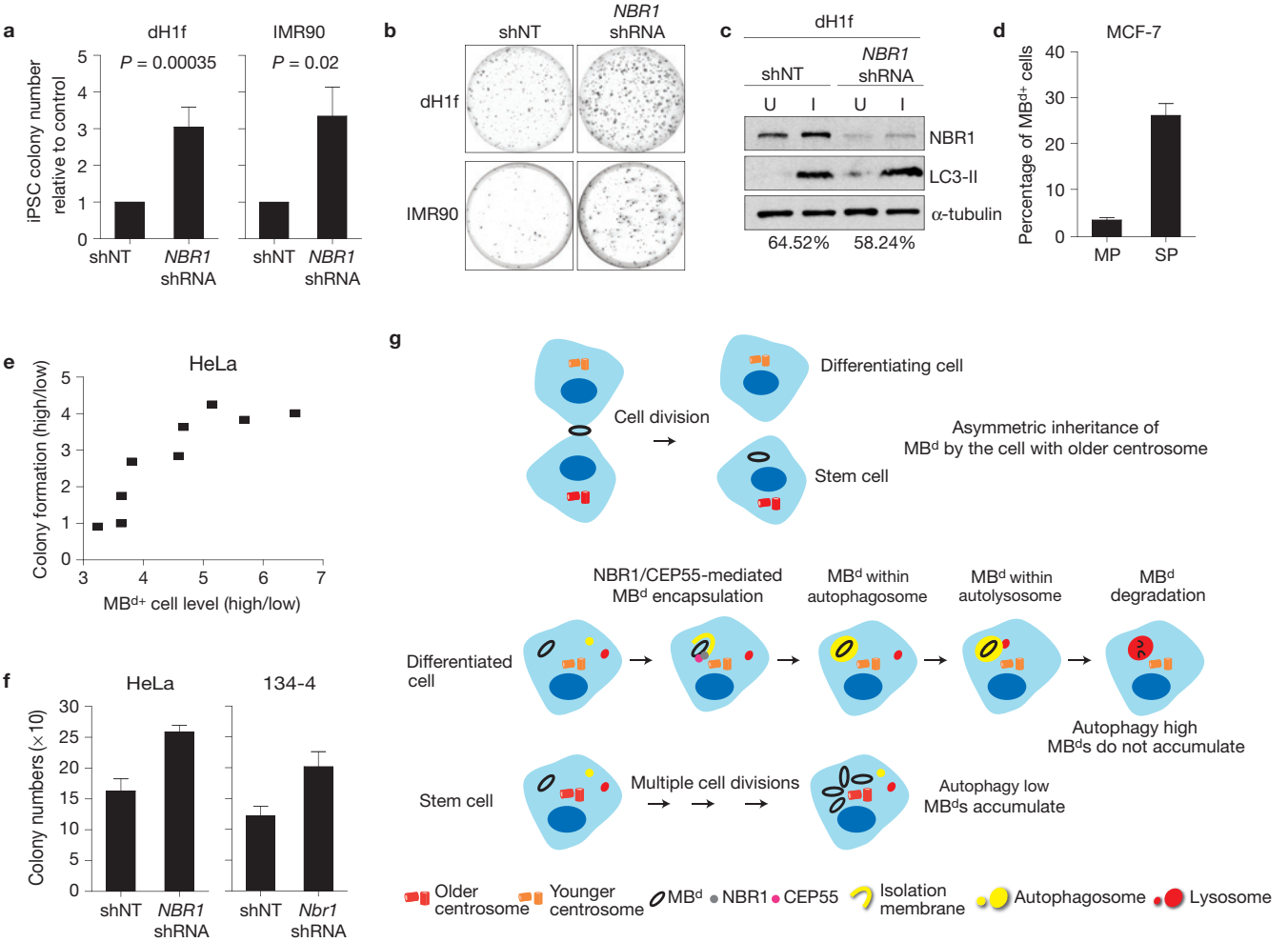

Figure 8 MB^d enrichment increases reprogramming efficiency and enhances *in vitro* tumorigenicity. (**a**–**c**) Reprogramming is more efficient after MB^d enrichment. Differentiated cells (dH1f) and embryonic fibroblasts (IMR90) are reprogrammed after stable expression of either *NBR1* shRNA or shNT. Emerging iPSC colonies are scored on the basis of TRA-1-60 expression[37]. Cells depleted of NBR1 to increase MB^d levels show an increase in iPSC colony formation (**a**,**b**, dH1f, 3.1 ± 0.5-fold, $n = 15$, $P = 0.00035$; IMR90, 3.4 ± 0.8-fold, $n = 3$, $P = 0.02$; data are mean ± s.e.m.) but insignificant changes in autophagic activity (**c**) over shNT control. (**b**) Representative plates with TRA-1-60-immunostained iPSC colonies. The immunoblot (**c**, top) and densitometry (**c**, bottom; percentage of autophagic flux) show representative results ($n = 3$); α-tubulin, loading control. (**d**) MCF-7 side-population (SP) cells have a significantly higher percentage of MB^{d+} cells over the non-side-population (MP; $P = 0.0015$, $n = 3$; data are mean ± s.d.). (**e**,**f**) MB^d enrichment in cancer cells leads to increased anchorage-independent growth. MKLP1–GFP-expressing HeLa cells are separated into 'MB^d-high' and 'MB^d-low' subpopulations. An increase in the 'MB^d high' over 'MB^d low' ratio is associated with an increase in soft-agar colony formation (**e**). No significant difference was observed when the enrichment of the MB^d-high subpopulation was less than threefold. More soft-agar colonies are formed when MB^{d}s are enriched by NBR1 depletion (*NBR1* shRNA) in HeLa (**f**, left; $P = 0.0012$, $n = 3$) and mouse 134-4 cells (**f**, right; $P = 0.0086$, $n = 3$); control, shNT. Data are mean ± s.d., and the colony number (**e**,**f**) is the sum of INT-violet-stained colonies from ten random fields. (**g**) Model for MB^d fate in cells. The newly formed MB^d is preferentially inherited by the daughter cell with the older centrosome (top panel). The inherited MB^d (black ring) is recognized by binding of the NBR1 autophagic receptor (grey circle) with the midbody protein CEP55 (magenta). The MB^d is then encapsulated by the autophagosome (yellow circle), and degraded after fusion of autophagosome and lysosome (red circle) in differentiated cells. This pathway prevents MB^d accumulation. In contrast, stem cells efficiently accumulate MB^{d}s through successive divisions and evasion of NBR1-mediated autophagy. Furthermore, differentiated and stem cells possess overall high and low autophagic activity, respectively. Uncropped images of blots are shown in Supplementary Fig. S6.

Our data identify two primary mechanisms for MB^d accumulation. The first is asymmetric MB^d inheritance by the daughter cell with the older centrosome (Fig. 8g, top). In fly testes and mouse neocortex, the old centrosome segregates to the stem cell during asymmetric divisions and is accompanied by increased microtubule-anchoring ability[4–6]. MB^d inheritance could be facilitated through increased anchoring of microtubules to the older centrosome, and increased microtubule binding to the MB^d in the daughter cell with the older centrosome. This would be consistent with the observed MB^d accumulation in stem cells but not in their differentiated progeny. Despite the slower division rate of stem cells *in vivo*[59], MB^d accumulation could still occur by this mechanism. However, our results also indicate that such asymmetry occurs in different cell types, indicating that it may only be physiologically relevant in stem cells and CSCs.

Evasion of autophagic degradation is a second mechanism for MB^d accumulation (Fig. 8g, bottom). This is exemplified by the inverse relationship between MB^d levels and autophagic activity, and by changes in MB^d levels with manipulation of autophagy

levels. MB^d accumulation can also be mediated by uncoupling receptor-mediated entry into the autophagy pathway, because depletion of the NBR1 autophagic receptor or overexpression of the corresponding ligand, CEP55, increases MB^d levels. In contrast, another known autophagic receptor, p62, does not seem to be involved in MB^d clearance (Fig. 7b,c). NBR1 and p62 can form a complex[53,60]; however, evidence indicates that they may act independently as autophagic receptors[53]. Thus, p62–NBR1 complex formation may not be a prerequisite for autophagic degradation. Because *NBR1* silencing increases MB^{d}s to levels seen following inhibition of autophagy in HeLa cells (Figs 6b and 7b), NBR1-mediated autophagic degradation probably represents a major pathway for selective MB^d elimination. However, it is still possible that other autophagic receptors and MB^d ligands may exist and contribute to MB^d degradation, even though CEP55 is the sole midbody ligand for the NBR1 receptor identified thus far (Fig. 7d). In our model, CEP55 and NBR1, and perhaps other MB^d ligands and autophagy receptors, act as switches that control MB^d fate. Ongoing proteomic analyses may identify other molecules and pathways for MB^d degradation.

MB^d levels can be further increased in autophagy-compromised *Atg5*$^{-/-}$ MEFs when lysosome enzymes are inhibited (data not shown), indicating that other degradative pathways may contribute to MB^d degradation. Chaperone-mediated autophagy[15,61], which targets ~30% of cytosolic proteins and is upregulated on compromised autophagy[62], is a potential candidate because multiple midbody proteins contain chaperone-mediated autophagy-targeting motifs (KFERQ-like motifs)[61]. The proteasome system is another major cellular degradation pathway[63] but it does not seem to play any role in MB^d degradation (Supplementary Fig. S5).

Other non-degradative processes may also regulate MB^d levels. Even though elevated proliferation rate has been proposed as a factor hindering autophagic MB^d degradation and causing MB^d accumulation in cancer and normal cells[12], we did not observe such a correlation (Fig. 4a). Further work is required to determine if MB^d accumulation also requires selective sequestration of previously inherited (pre-existing) MB^{d}s, as indicated by selective accumulation of MB^{d}s in stem cells of the testes and lateral ventricle of the brain (Fig. 3a–d). Release of MB^{d}s has also been observed in chicken and mouse neural progenitors[13,14] and in human cells (ref. 8 and Fig. 1g), and may be another, possibly minor, pathway for eliminating MB^{d}s (or for intercellular signalling[14]). Finally, ongoing work is addressing whether MB^{d}s are distributed to both daughters of stem cells during symmetric divisions, as might be expected if MB^{d}s are essential for stem-cell function.

In summary, our results demonstrate that MB^{d}s are more than the remnants of cytokinesis. Their fate is differentially controlled in different cell types and mediated by diverse pathways. The shared ability to accumulate MB^{d}s by stem cells and putative CSCs, and the striking impact on cellular phenotypes following manipulation of MB^d levels, indicate that MB^{d}s carry out important cell-type-specific functions that remain to be discovered. □

METHODS

Methods and any associated references are available in the online version of the paper at http://www.nature.com/naturecellbiology

Note: Supplementary Information is available on the Nature Cell Biology website

ACKNOWLEDGEMENTS

We thank E. Baehrecke for critical reading of the manuscript, T. Schlaeger and colleagues for assistance with H1-OGN and associated cell lines, the University of Massachusetts Medical School (UMMS) Flow Facility for assistance with MB^d enrichment, P. Furcinitti of UMMS Digital Light Microscopy Core Facility for assistance with imaging, the UMMS DERC Morphology Core for assistance with immunohistochemitry, D. Guertin and C. Sparks for assistance with SMP preparation, S. Lyle and C. Powers for performing EM experiments and H-L. Liu for assistance with clone construction. We thank N. Mizushima for GFP–LC3-expressing *Atg5*$^{-/-}$ and matched wild-type MEFs, M. Komatsu and T. Ishii for *p62*$^{-/-}$ and matched wild-type MEFs, S. Jones for *ex vivo* C57BL/6 MEFs, B. Lewis for mouse hepatocellular cancer lines, S. Pino for *in vitro* activated T cells, W. Jiang for MKLP1–GFP plasmid, K. Khanna for CEP55–eGFP plasmid, J. Lippincott-Schwartz and G. Gaietta for plasmids for FPP assay, B. Levine (UT Southwestern) for Flag-tagged BECN1-expressing plasmid, A. Khodjakov for CETN1–GFP-expressing plasmids, K. Lee for hCenexin1 antibody and the Progeria Society for cell lines. The α6F antibody to Na/K-ATPase developed by D. M. Fambrough and the H4B4 antibody to LAMP2 developed by J.T. August and J. E. K. Hildreth were obtained from the Developmental Studies Hybridoma Bank developed under the auspices of the National Institute of Child Health and Human Development and maintained by The University of Iowa, Department of Biology. This work was supported by funding from the National Institutes of Health (GM051994 to S.D. and F32 GM084660-02 to D.B.), the W.M. Keck Foundation to S.D., the Ellison Foundation (AG-SS-1918-07) to S.D., the Department of Defense (W81XWH-08-1-0457 to S.D. and W81XWH-06-1-0140 to C-T.C.) and the Diabetes and Endocrine Resource Center (5P30DK3252025). Core resources supported by the Diabetes Endocrinology Research Center grant DK32520 were also used.

AUTHOR CONTRIBUTIONS

C-T.C. and S.D. conceived the project and wrote the manuscript with the help of T-C.K. and D.B. The experiments on the inheritance and localization of MB^{d}s as well as some for MB^d degradation were conducted by C-T.C. The experiments on MB^d accumulation were conducted by C-T.C. with the help of T-C.K. and C.M.W. Investigation of the mechanisms for MB^d degradation was conceived by T-C.K. and S.D., and much of the work executed by T-C.K. Autophagic flux assay, soft-agar assay of FACS-isolated cells and MB^d localization in neural progenitors were conducted by D.B., who contributed substantially to the work and intellectual input on multiple aspects of this project. The reprogramming assay was conducted and analysed by T-C.K., T.T.O and S.L. The preparation of hESCs for live imaging was conducted by S.A. Tissue preparation was assisted by P.X. and J.M.H.

COMPETING FINANCIAL INTERESTS

The authors declare no competing financial interests.

Published online at http://www.nature.com/naturecellbiology
Reprints and permissions information is available online at http://www.nature.com/reprints

1. Eggert, U. S., Mitchison, T. J. & Field, C. M. Animal cytokinesis: from parts list to mechanisms. *Annu. Rev. Biochem.* **75,** 543–66 (2006).
2. Neumüller, R. A. & Knoblich, J. A. Dividing cellular asymmetry: asymmetric cell division and its implications for stem cells and cancer. *Genes Dev.* **23,** 2675–2699 (2009).
3. Doxsey, S., McCollum, D. & Theurkauf, W. Centrosomes in cellular regulation. *Annu. Rev. Cell Dev. Biol.* **21,** 411–434 (2005).
4. Yamashita, Y. M., Mahowald, A. P., Perlin, J. R. & Fuller, M. T. Asymmetric inheritance of mother versus daughter centrosome in stem cell division. *Science* **315,** 518–521 (2007).
5. Wang, X. *et al.* Asymmetric centrosome inheritance maintains neural progenitors in the neocortex. *Nature* **461,** 947–955 (2009).
6. Yamashita, Y. M., Jones, D. L. & Fuller, M. T. Orientation of asymmetric stem cell division by the APC tumor suppressor and centrosome. *Science* **301,** 1547–1550 (2003).
7. Barr, F. A. & Gruneberg, U. Cytokinesis: placing and making the final cut. *Cell* **131,** 847–860 (2007).
8. Mullins, J. M. & Biesele, J. J. Terminal phase of cytokinesis in D-98s cells. *J. Cell Biol.* **73,** 672–684 (1977).
9. Gromley, *et al.* Centriolin anchoring of exocyst and SNARE complexes at the midbody is required for secretory-vesicle-mediated abscission. *Cell* **123,** 75–87 (2005).
10. Steigemann, P. *et al.* Aurora B-mediated abscission checkpoint protects against tetraploidization. *Cell* **136,** 473–484 (2009).
11. Goss, J. W. & Toomre, D. K. Both daughter cells traffic and exocytose membrane at the cleavage furrow during mammalian cytokinesis. *J. Cell Biol.* **181,** 1047–1054 (2008).

12. Pohl, C. & Jentsch, S. Midbody ring disposal by autophagy is a post-abscission event of cytokinesis. *Nat. Cell Biol.* **11,** 65–70 (2009).
13. Marzesco, A. M. *et al.* Release of extracellular membrane particles carrying the stem cell marker prominin-1 (CD133) from neural progenitors and other epithelial cells. *J. Cell Sci.* **118,** 2849–2858 (2005).
14. Dubreuil, V. *et al.* Midbody and primary cilium of neural progenitors release extracellular membrane particles enriched in the stem cell marker prominin-1. *J. Cell. Biol.* **176,** 483–495 (2007).
15. Mizushima, N., Levine, B., Cuervo, A. M. & Klionsky, D. J. Autophagy fights disease through cellular self-digestion. *Nature* **451,** 1069–1075 (2008).
16. Mizushima, N. & Klionsky, D. Protein turnover via autophagy: implications for metabolism. *Annu. Rev. Nutr.* **27,** 19–40 (2007).
17. Yorimitsu, T. & Klionsky, D. J. Eating the endoplasmic reticulum: quality control by autophagy. *Trends Cell Biol.* **17,** 279–285 (2007).
18. Levine, B. & Kroemer, G. Autophagy in the pathogenesis of disease. *Cell* **132,** 27–42 (2008).
19. Kuma, A. *et al.* The role of autophagy during the early neonatal starvation period. *Nature* **432,** 1032–1036 (2004).
20. Fimia, G. M. *et al.* Ambra1 regulates autophagy and development of the nervous system. *Nature* **447,** 1121–1125 (2007).
21. Tsukamoto, S. *et al.* Autophagy is essential for preimplantation development of mouse embryos. *Science* **321,** 117–120 (2008).
22. Cecconi, F. & Levine, B. The role of autophagy in mammalian development: cell makeover rather than cell death. *Dev. Cell* **15,** 344–357 (2008).
23. Hara, T. *et al.* Suppression of basal autophagy in neural cells causes neurodegenerative disease in mice. *Nature* **441,** 885–889 (2006).
24. Komatsu, M. *et al.* Impairment of starvation-induced and constitutive autophagy in Atg7-deficient mice. *J. Cell Biol.* **169,** 425–434 (2005).
25. Rujano, M. A. *et al.* Polarised asymmetric inheritance of accumulated protein damage in higher eukaryotes. *PLoS Biol.* **4,** 2325–2335 (2006).
26. Johnston, J. A., Illing, M. E. & Kopito, R. R. Cytoplasmic dynein/dynactin mediates the assembly of aggresomes. *Cell. Motil. Cytoskeleton* **53,** 26–38 (2002).
27. Anderson, C. T. & Stearns, T. Centriole age underlies asynchronous primary cilium growth in mammalian cells. *Curr. Biol.* **19,** 1498–1502 (2009).
28. Piel, M., Meyer, P., Khodjakov, A., Rieder, C. L. & Bornens, M. The respective contributions of the mother and daughter centrioles to centrosome activity and behavior in vertebrate cells. *J. Cell Biol.* **149,** 317–330 (2000).
29. Oatley, J. M. & Brinster, R. L. Regulation of spermatogonial stem cell self-renewal in mammals. *Annu. Rev. Cell Dev. Biol.* **24,** 263–286 (2008).
30. Barroca, V. *et al.* Mouse differentiating spermatogonia can generate germinal stem cells *in vivo*. *Nat. Cell Biol.* **11,** 190–196 (2009).
31. Bilgüvar, K. *et al.* Whole-exome sequencing identifies recessive WDR62 mutations in severe brain malformations. *Nature* **467,** 207–210 (2010).
32. Morris, R. J. *et al.* Capturing and profiling adult hair follicle stem cells. *Nat. Biotechnol.* **22,** 411–417 (2004).
33. Conboy, M. J., Cerletti, M., Wagers, A. J. & Conboy, I. M. Immuno-analysis and FACS sorting of adult muscle fiber-associated stem/precursor cells. *Methods Mol. Biol.* **621,** 165–173 (2010).
34. Park, I. H. *et al.* Reprogramming of human somatic cells to pluripotency with defined factors. *Nature* **451,** 141–146 (2008).
35. Chan, E. M. *et al.* Live cell imaging distinguishes bona fide human iPS cells from partially reprogrammed cells. *Nat. Biotechnol.* **27,** 1033–1037 (2009).
36. Zwaka, T. P. & Thomson, J. A. Homologous recombination in human embryonic stem cells. *Nat. Biotechnol.* **21,** 319–321 (2003).
37. Visvader, J. E. & Lindeman, G. J. Cancer stem cells in solid tumours: accumulating evidence and unresolved questions. *Nat. Rev. Cancer* **8,** 755–768 (2008).
38. O'Brien, C. A., Pollett, A., Gallinger, S. & Dick, J. E. A human colon cancer cell capable of initiating tumour growth in immunodeficient mice. *Nature* **445,** 106–110 (2007).
39. Pece, S. *et al.* Biological and molecular heterogeneity of breast cancers correlates with their cancer stem cell content. *Cell* **140,** 62–73 (2010).
40. Pardal, R., Clarke, M. F. & Morrison, S. J. Applying the principles of stem-cell biology to cancer. *Nat. Rev. Cancer* **3,** 895–902 (2003).
41. Salic, A. & Mitchison, T. J. A chemical method for fast and sensitive detection of DNA synthesis *in vivo*. *Proc. Natl Acad. Sci. USA* **105,** 2415–2420 (2008).
42. Lorenz, H., Hailey, D. W. & Lippincott-Schwartz, J. Fluorescence protease protection of GFP chimeras to reveal protein topology and subcellular localization. *Nat. Methods* **3,** 205–210 (2006).
43. Eskelinen, E. L., Tanaka, Y. & Saftig, P. At the acidic edge: emerging functions for lysosomal membrane proteins. *Trends Cell Biol.* **13,** 137–145 (2003).
44. Klionsky, D. J. *et al.* Guidelines for the use and interpretation of assays for monitoring autophagy in higher eukaryotes. *Autophagy* **4,** 151–175 (2008).
45. Liang, X. H. *et al.* Induction of autophagy and inhibition of tumorigenesis by beclin 1. *Nature* **402,** 672–676 (1999).
46. Sato, K. *et al.* Autophagy is activated in colorectal cancer cells and contributes to the tolerance to nutrient deprivation. *Cancer Res.* **67,** 9677–9684 (2007).
47. Sarkar, S. *et al.* A rational mechanism for combination treatment of Huntington's disease using lithium and rapamycin. *Hum. Mol. Genet.* **17,** 170–178 (2008).
48. Sarkar, S. *et al.* Lithium induces autophagy by inhibiting inositol monophosphatase. *J. Cell Biol.* **170,** 1101–1111 (2005).
49. Mizushima, N. & Yoshimori, T. How to interpret LC3 immunoblotting. *Autophagy* **3,** 542–545 (2007).
50. Bjorkoy, G. *et al.* p62/SQSTM1 forms protein aggregates degraded by autophagy and has a protective effect on huntingtin-induced cell death. *J. Cell Biol.* **171,** 603–614 (2005).
51. Komatsu, M. *et al.* Homeostatic levels of p62 control cytoplasmic inclusion body formation in autophagy-deficient mice. *Cell* **131,** 1149–1163 (2007).
52. Pankiv, S. *et al.* p62/SQSTM1 binds directly to Atg8/LC3 to facilitate degradation of of ubiquitinated protein aggregates by autophagy. *J. Biol. Chem.* **282,** 24131–24145 (2007).
53. Kirkin, V. *et al.* A role for NBR1 in autophagosomal degradation of ubiquitinated substrates. *Mol. Cell* **27,** 505–516 (2009).
54. Waters, S. *et al.* Interactions with LC3 and polyubiquitin chains link nbr1 to autophagic protein turnover. *FEBS Lett.* **583,** 1846–1852 (2009).
55. Yu, J. *et al.* Induced pluripotent stem cell lines derived from human somatic cells. *Science* **318,** 1917–1920 (2007).
56. Engelmann, K., Shen, H. & Finn, O. J. MCF7 side population cells with characteristics of cancer stem/progenitor cells express the tumor antigen MUC1. *Cancer Res.* **68,** 2419–2426 (2008).
57. Zhang, Y. *et al.* SEPA-1 mediates the specific recognition and degradation of P granule components by autophagy in *C. elegans*. *Cell* **136,** 308–321 (2009).
58. Strome, S. Specification of the germ line. *WormBook* **28,** 1–10 (2005).
59. Fuchs, E. The tortoise and the hair: slow-cycling cells in the stem cell race. *Cell* **137,** 811–819 (2009).
60. Lamark, T. *et al.* Interaction codes within the family of mammalian Phox and Bem1p domain-containing proteins. *J. Biol. Chem.* **278,** 34568–34581 (2003).
61. Majeski, A. E. & Dice, J. F. Mechanisms of chaperone-mediated autophagy. *Int. J. Biochem. Cell Biol.* **36,** 2435–2444 (2004).
62. Kaushik, *et al.* Constitutive activation of chaperone-mediated autophagy in cells with impaired macroautophagy. *Mol. Biol. Cell* **19,** 2179–2192 (2008).
63. Nedelsky, N. *et al.* Autophagy and the ubiquitin–proteasome system: collaborators in neuroprotection. *Biochim. Biophys. Acta.* **1782,** 691–699 (2008).

DOI: 10.1038/ncb2332

METHODS

Cell lines. hESC and iPSC lines include H1 (WA01), H9 (WA09), H1-OGN (Oct4–eGFP knock-in H1; ref. 36) and dH1f-iPS (ref. 34), which is reprogrammed from dH1f cells differentiated from H1-OGN (HSCI at Children's Hospital Boston). Differentiated lines include hRPE-1 (Clontech), MCF-10A, adult human fibroblasts (PCS-201-012, ATCC), hFib2 (ref. 34), IMR90 (CCL-186, ATCC), *ex vivo* C57BL/6 MEFs, GFP–LC3-expressing $Atg5^{-/-}$ and $Atg5^{+/+}$ MEFs (ref. 19), and $p62^{-/-}$ and $p62^{+/+}$ MEFs (ref. 51). Cancer cell lines include DLD-1, HeLa, NCC-IT, PC-3, U2OS, SAOS-2, 134-4, MCF-7, MCF-10AT and MCF-10CA1a. Mouse SMPs (ref. 33) and *in vitro* activated T cells were isolated and stimulated following standard protocols. Cells were used within four (primary cultures) or ten (established cell lines, hESCs and iPSCs) passages. Cells expressing MKLP1–GFP, monomeric RFP and CETN1–GFP were created in the present study or ref. 28.

Immunofluorescence and immunohistochemistry. Immunofluorescence was carried out as described[9,13,64]. To label lysosomes and autophagosomes, cells were permeabilized with 0.05% saponin in blocking buffer (10% goat serum–PBS). Preparations for immunohistochemistry were fixed with 4% paraformaldehyde–0.5% glutaraldehyde by perfusion. Testes were processed and stained following 2–4 h post-fixation with 4% paraformaldehyde. Midbody-derived rings between spermatocyte syncytia[65] were observed if stained longer. Images were taken on a Zeiss Axioskop 2 microscope, a Zeiss Axiovert 200 microscope with a PerkinElmer UltraView LAS spinning disc, or an Olympus BX-51 microscope. Images were processed and analysed with MetaMorph (Molecular Devices) and Imaris (Bitplane).

Electron microscopy. For conventional electron microscopy, Mouse tissue, fixed with 5% glutaraldehyde in 50 mM sodium cacodylate buffer (pH = 7.4) for 30 min by perfusion, was diced into 1 mm cubes for 1 h post-fixation at 4 °C. Cubes were washed with cacodylate buffer, stained and embedded in Spi-pon/Araldite, and sectioned at 70–500 nm before staining with 25% uranyl acetate and Reynold's lead citrate. Images were taken on a Philips CM12 electron microscope with an Erlangshen CCD (charge-coupled device) camera (Gatan).

For immunogold electron microscopy, MCF-7 cells on coverslips were pre-permeabilized for 60 s with preperm buffer (80 mM PIPES at pH 6.8, 0.5 mM EGTA, 1 mM MgCl, 0.5% Triton X-100), fixed with 4% paraformaldehyde for 10 min, labelled for MKLP1 for 1 h, processed as described[66] using 12 nm gold-conjugated goat anti-rabbit IgG (Jackson ImmunoResearch) and embedded in Spi-pon/Araldite. 80 nm sections were cut, stained and viewed as above.

Time-lapse imaging. CETN1–GFP-expressing lines were grown on 35 mm MatTek dishes (MatTek) or coverslips before imaging[9]. H9 hESCs were seeded on matrigel-coated dishes overnight, then transduced with CETN1–GFP and grown for more than 72 h in complete mTeSR1 medium (Stemcell Technologies). The transduced cells were imaged every 15 min in phenol red-free DMEM/F12 medium (Invitrogen) with mTeSR1 supplement and 10 mM HEPES, and stained to confirm MB^d inheritance. Duplicate dishes of transduced cells were stained for stem-cell markers to ensure cell quality.

MB^d quantification. Quantification was based on the markers that: (1) labelled both mitotic midbodies and MB^ds (MKLP1, MgcRacGAP or CEP55); (2) labelled midbodies differently from MB^ds (α-tubulin or Aurora B); (3) defined cell boundaries (α-tubulin or ZO-1). Because CEP55, MKLP1 and MgcRacGAP also label centrioles and spindle midzones, cells were co-stained with centrosome antibody (for example 5051), and a size threshold for midbodies/MB^ds (1 μm) was introduced to exclude non-MB^d structures. Structures with midbody-specific or non-midbody/MB^d labelling were excluded from MB^d counts. For hESC cell counts, 5–11 colonies were imaged from triplicates in each experiment. For other cell types, random fields were imaged until $n > 500$ cells. Each dividing cell was considered one cell.

Doubling-time calculations. Cells were seeded ($1–1.5 \times 10^5$ per 60 mm dish), and total cell counts were taken by haemocytometer every 24 h for four days. Alternatively, cells were seeded ($2.5–5.0 \times 10^3$ per well, 96-well plates), and the absorbance from an MTS-based colorimetric assay (no G3582; Promega) was used to estimate cell counts every 24 h. Time versus $\log_{10}$(average cell counts or absorbance at that time) was plotted and the slope ascertained. Population doubling time $T_{1/2} = \log_{10}(2)/\text{slope}$. For some cell lines, both methods were used and gave similar results.

MB^d localization assays. For the extracellular trypsin treatment assays, MKLP1–GFP-expressing HeLa cells grown in MatTek dishes were imaged every 3 min, and underwent no morphological changes on replacement of media with PBS. After trypsin addition, GFP^+ MB^ds were monitored for 60–90 min for intensity reduction (degradation) or detachment from cells (dissociation).

For the co-culture assays, equal numbers of monomeric RFP- or MKLP–GFP-expressing cells were seeded and co-cultured in 60 mm dishes with coverslips. Cells were stained two days later, and the percentage of GFP^+ MB^ds associated with RFP^+ cells was determined.

The FPP assay was carried out as reported[42] except that cells were plated in MatTek dishes 24 h before co-transfection of MKLP1–GFP and GAPDH–dsRed (Lipofectamine 2000, Invitrogen). Cells were permeabilized and then digested with proteinase K (50 μg ml^{-1}). Constructs labelling mitochondria, peroxisomes, endoplasmic reticulum and Golgi were used as controls.

Lysosome and proteasome assays. Cells at 70% confluency were incubated with chloroquine (200 μM–PBS; Sigma), E64d + pepstatin A (E64d–PepA) (10 μg ml^{-1}–DMSO each; Sigma)[44,51] or solvents alone (controls) for 22 h before fixation. Lysosome inhibition was confirmed and visualized after 12 h DQ-Red BSA (10 μl ml^{-1}; Invitrogen) incubation. Mitotic hRPE-1 cells were treated with proteasome inhibitors MG132 (1 μM; Sigma) or lactacystin (50 μM; Sigma) 1 h after replating.

Autophagy-manipulation assays. MB^ds were quantified in more than 500 cells in triplicate unless otherwise noted.

siRNAs targeting human ATG7 (ref. 67), p62 (ref. 12), NBR1 (ref. 53) (2,503–2,521 base pairs (bp), GenBank NM 005899), Lamin A/C (ref. 9) and GFP (5′-NNCAUGAAGCAGCACGACUUC-3′) were from Dharmacon. MB^d levels were analysed 48 h after 1 nmol siRNA transfection (Oligofectamine, Invitrogen). For NBR1 and p62 experiments, only cells negative for p62 and/or NBR1 immunofluorescence were analysed.

For the *BECN1* overexpression assays, MB^d levels were analysed in 265 $Flag^+$ and 2,200 control MCF-7 cells 48 h after Flag–BECN1 (4 μg) or mock nucleofection (Amaxa).

LiCl + rapamycin treatment. MB^d levels in HeLa cells were examined 24 h after treatment with LiCl (10 mM; Sigma) and rapamycin (200 nM; Calbiochem) or with DMSO.

For the *CEP55–eGFP* overexpression assays, MB^d levels and their NBR1 association were assessed in hRPE-1 cells (1×10^5 per well, six-well plates) 48 h after CEP55–eGFP (1 μg), eGFP (1 μg) or mock transfection.

Biochemical assays. Protease and phosphatase inhibitors, cell lysates, SDS–PAGE and immunoblotting were purchased or carried out as described[9] unless specified.

Autophagic flux was determined in the following manner. Lysates of E64d–PepA (I)- and DMSO (U)-treated cells were blotted for α-tubulin and LC3. LC3-II levels were determined and normalized to α-tubulin using ImageJ. Autophagic flux = $|100 - ((U/ILC3 - IIlevel) \times 100)|$.

For immunoprecipitation assays, hRPE-1 cell lysates (50 mM Tris-HCl at pH 7.5, 150 mM NaCl, 2 mM EDTA, 1 mM EGTA, 1% Triton X-100, 10% glycerol, 4 °C) were pre-cleared for 1 h with protein G-plus conjugated agarose beads (Santa Cruz) at 4 °C, incubated with 2 μg normal IgG, anti-CEP55 or anti-NBR1 antibodies for 3 h at 4 °C and incubated overnight at 4 °C with 25 ml protein G-plus beads. Following washes with lysis buffer and elution, immunoprecipitated proteins were analysed by SDS–PAGE and immunoblotting.

Assays for MB^d function. For cellular reprogramming assays, viral production, transduction and reprogramming were carried out as described[34,35,55,68]. Commercially available shRNA against NBR1 (pSM2c-*NBR1* shRNA, V2MM_36901; 4–22 bp, GenBank NM 005899) was cloned into pGIPZ lentiviral vector (Open Biosystems). Embryonic fibroblasts (IMR90), adult fibroblasts (hFib2) and dH1f cells were transduced with either NBR1-specific or non-targeting shRNA vector, and puromycin-selected to establish NBR1-depleted (*NBR1* shRNA) and control (shNT) lines. dH1f cells (2.5×10^4 per assay) were reprogrammed with lentiviral vectors[69] (Addgene no 21162 and 21164) expressing *OCT4*, *SOX2*, *KLF4* and *c-MYC* (refs 34,35,68), whereas the reprogramming of IMR90 and hFib2 cells (5×10^4 per assay) also included lentiviral vectors expressing Nanog and Lin28 (refs 55,69; Addgene no 21163). iPSC colonies were quantified on day 21 on the basis of TRA-1-60 expression using ImageJ, as reported[35,68], and with parameters ≥148 (threshold), 0.5–1 (circularity) and either 10–infinity or 30–infinity (size).

The side-population assays were carried out as previously described[56] in MCF-7 cells. The MB^d levels in side- and non-side-populations were determined as described above.

For the soft-agar assays, 'MB^d-high' and 'MB^d-low' subpopulations of MKLP1–GFP-expressing HeLa cells were separated by FACS, and plated in soft agar (2.5×10^4 per well, six-well plates). The MB^d levels were determined 12–15 h after plating aliquots of subpopulations onto coverslips. For the *NBR1*-silencing soft-agar assay, NBR1-depleted (*NBR1* shRNA) and control (shNT) cells (1×10^5 per 100 mm dish) were plated. For both assays, cells were grown for ~3 weeks at 37 °C, and stained as described[70]. Colonies were quantified microscopically, and the average from triplicate wells or plates presented.

Antibodies. Antibodies to the following proteins/tags were used in this study: Atg5 (1:2,000, Cosmo Bio, CAC-TMD-PH-ATG); ATG7 (1:1,000, ProSci, 3617); Actin (1:300, Sigma, AC-40); Aurora B (1:100, BD TRAns Lab, 611082); CD13 (1:50, BioLegend, 301707); CD133 (1:200, eBioscience, 14-1331); CEP55 (1:50, 1:100 and 1:1,000 for immunofluorescence, Abnova no H00055165-B01, Abnova no H00055165-A01 and a gift from K. Kurtche, respectively; 1:500 for immunoblotting, Genetax no GTX112190); hCenexin1 (1:100, a gift from K.S. Lee); Centriolin (1:200, ref. 9); Flag (1:200, Sigma, F7425); GAPDH (1:8,000; Santa Cruz, SC-32233); GFP (1:1,000; Abcam, ab6556, and Santa Cruz, sc-9996); GT335 (1:100; a gift from P. Denoulet); β1-integrin (1:50; BD Phramingen); K15 (1:100; Lab Vision, MS-1068-P); LC3 (1:10 for immunofluorescence, Nano Tools, LC3-5F10; 1:300 for immunoblotting, Novus Bio NB100-2331); LAMP2 (1:50, H4B4 from DSHB); MgcRacGAP (1:500, Abcam, ab2270); MKLP1 (1:1,000 for immunofluorescence, 1:200 for immunohistochemistry, 1:10 for immuno-electron microscopy, Santa Cruz, sc-867); NBR1 (1:500, Abnova, H00004077-B01P); p62, human samples (1:500, BD Trans Lab, 610833); p62, mouse samples (1:1,000, Progen, GP62-C); RFP (1:200, Clontech, 632496); Na/K-ATPase (1:15, α6F, DSHB); α-tubulin (1:100 for immunofluorescence, 1:400 for immunoblotting, Sigma, T9026a; 1:100 for immunofluorescence, Millipore, CBL270); α-tubulin–FITC (fluorescein isothiocyanate) (1:300, Sigma, F2168); TRA-1-60–biotin (1:200, eBioscience, 13-8863); ubiquitin (1:2,000, BD BioSci, no 550944); WGA-Alexa Fluor 555 (1:200, Molecular Probes, W32464); ZO-1–FITC (1:50, Zymed, 33-9111).

Statistics. Data were analysed by Student's one-tailed paired *t*-test or unpaired with Welch's correction unless specified. One-way analysis of variance was used in conjunction with Tukey's test for comparisons among multiple groups. For the EdU-labelling assay, the EdU intensity was first logarithmically transformed for the use of one-way analysis of variance. Statistically analysed experiments were completed at least three times.

64. Xu, P. & Davis, R. J. c-Jun NH2-terminal kinase is required for lineage-specific differentiation but not stem cell self-renewal. *Mol. Cell Biol.* **30,** 1329–1340 (2010).
65. Greenbaum, M. P., Ma, L. & Matzuk, M. M. Conversion of midbodies into germ cell intercellular bridges. *Dev. Biol.* **305,** 389–396 (2007).
66. Mitchison, T., Evans, L., Schulze, E. & Kirschner, M. Sites of microtubule assembly and disassembly in the mitotic spindle. *Cell* **45,** 515–527 (1986).
67. Yu, L. *et al.* Regulation of an ATG7-beclin 1 program of autophagic cell death by caspase-8. *Science* **304,** 1500–1502 (2004).
68. Loewer, S. *et al.* Large intergenic non-coding RNA-RoR modulates reprogramming of human induced pluripotent stem cells. *Nat. Genet.* **42,** 1113–1117 (2010).
69. Yu, J. *et al.* Human induced pluripotent stem cells free of vector and transgene sequences. *Science* **324,** 797–801 (2009).
70. Sachdev, S., Bu, Y. & Gelman, I. H. Paxillin-Y118 phosphorylation contributes to the control of Src-induced anchorage-independent growth by FAK and adhesion. *BMC Cancer* **12,** 9–12 (2009).

CORRIGENDUM

Midbody accumulation through evasion of autophagy contributes to cellular reprogramming and tumorigenicity

Tse-Chun Kuo, Chun-Ting Chen, Desiree Baron, Tamer T. Onder, Sabine Loewer, Sandra Almeida, Cara M. Weismann, Ping Xu, Jean-Marie Houghton, Fen-Biao Gao, George Q. Daley and Stephen Doxsey

Nat. Cell Biol. **13,** 1214–1223 (2011); published online 11 September 2011; corrected after print 15 November 2011

In the version of this article initially published online and in print, the first sentence in the Acknowledgements section was incorrect. The correct sentence is:

We thank E. Baehrecke for critical reading of the manuscript, T. Schlaeger and colleagues for assistance with H1-OGN and associated cell lines, the University of Massachusetts Medical School (UMMS) Flow Facility for assistance with MBd enrichment, P. Furcinitti of UMMS Digital Light Microscopy Core Facility for assistance with imaging, the UMMS DERC Morphology Core for assistance with immunohistochemitry, D. Guertin and C. Sparks for assistance with SMP preparation, S. Lyle and C. Powers for performing EM experiments and H-L. Liu for assistance with clone construction. This error has been corrected in the HTML and PDF versions of the article.

nature cell biology

DOI: 10.1038/ncb2332

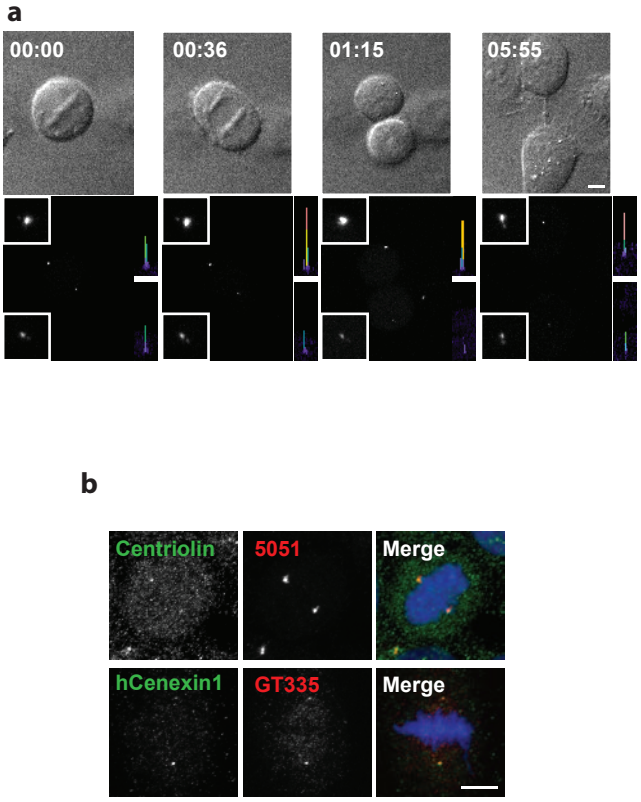

Figure S1 Different-aged centrosomes in dividing cells show differential labeling for the components and modification of centrosomes. (**a**) Older/more mature centrosome retains the brighter CETN1-GFP signal throughout the mitotic cell cycle. Left to right: metaphase, anaphase, telophase and cytokinesis. (**b**) The centrosome pairs in representative mitotic cells show differential labeling of centriolin (top panel, green), hCenexin1 (bottom panel, green) and glutamylated tubulin (GT335; bottom panel, red). Centriolin and hCenexin1 are markers for centriole maturation, and glutamylated tubulin for tubulin modification at centrioles, respectively. Centrosomes are labeled by human autoimmune antibody 5051 (top panel, red). DAPI stains DNA (blue). Bar, 5 μm.

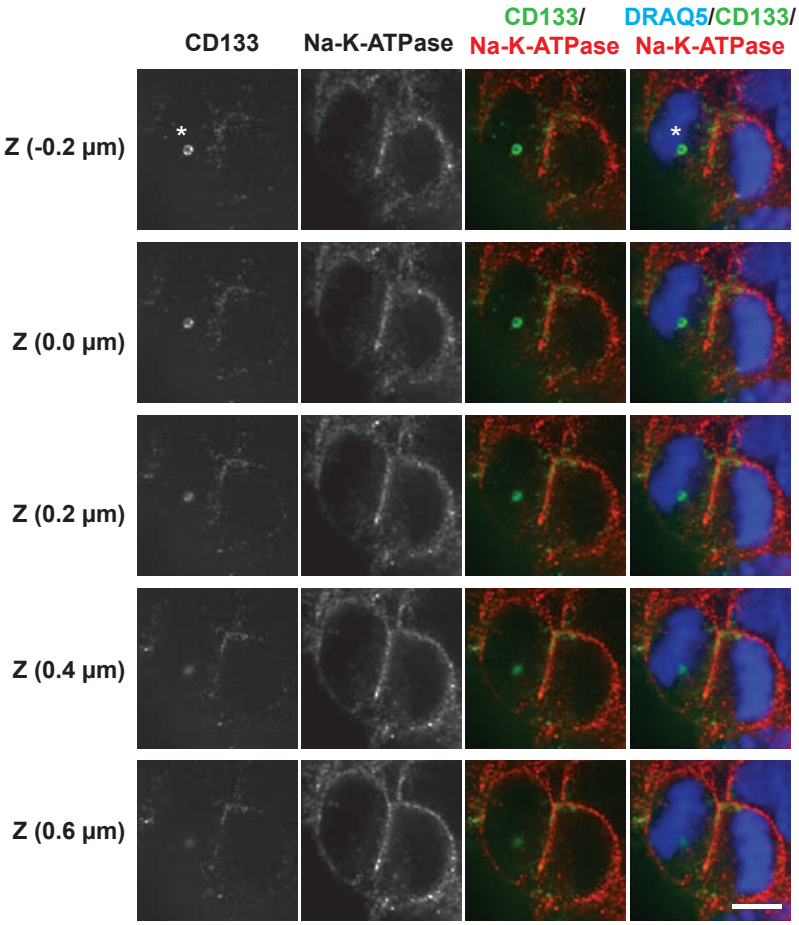

Figure S2 Multiple planes of confocal images demonstrate that the MB^d (asterisk) in the ventricle-facing daughter of the dividing neural progenitor is intracellular (also shown in Fig. 3d). CD133, MB/MB^d marker (green); Na-K-ATPase, cell-border marker (red); DRAQ5, DNA (blue); Bar, 5 μm.

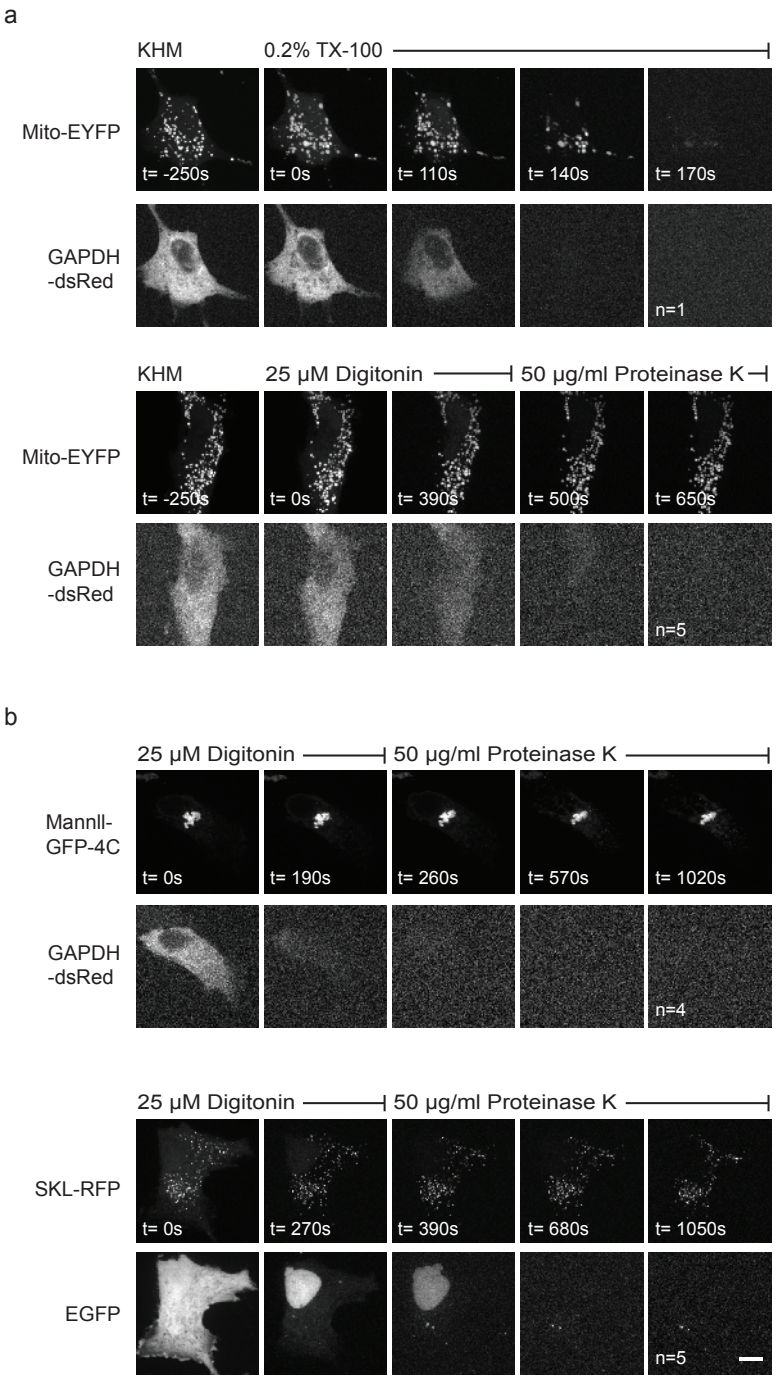

Figure S3 Organelles respond to digitonin treatment as expected. (**a, b**) Membranous organelles are not disrupted during digitonin-mediated permeabilization in FPP assays. (a) hRPE-1 cells expressing Mito-EYFP to label mitochondria, and GAPDH-dsRed to mark cytoplasm, are pre-incubated in KHM buffer (110 mM potassium acetate, 20 mM HEPES, 2 mM $MgCl_2$), and then treated either with 0.2% TX-100 (top panel) or with 25 µM digitonin (bottom panel). TX-100 releases both GAPDH and Mito-EYFP from cells, whereas digitonin releases only GAPDH and does not disrupt mitochondrial integrity as shown by the retention of Mito-EYFP in the presence of Proteinase K. (b) hRPE-1 cells expressing MannII-GFP-4C, a Golgi complex marker (top panel), or SKL-RFP, a peroxisome marker (bottom panel), are treated with digitonin followed by proteinase K digestion as in (a). The fluorescent proteins in Golgi complex and peroxisomes are resistant to proteinase K digestion after digitonin-mediated permeablization, showing that the Golgi complex and peroxisomes are intact. Other organelles were also examined to ensure their integrity. Similar results were observed in HeLa cells. Bar, 5 µm.

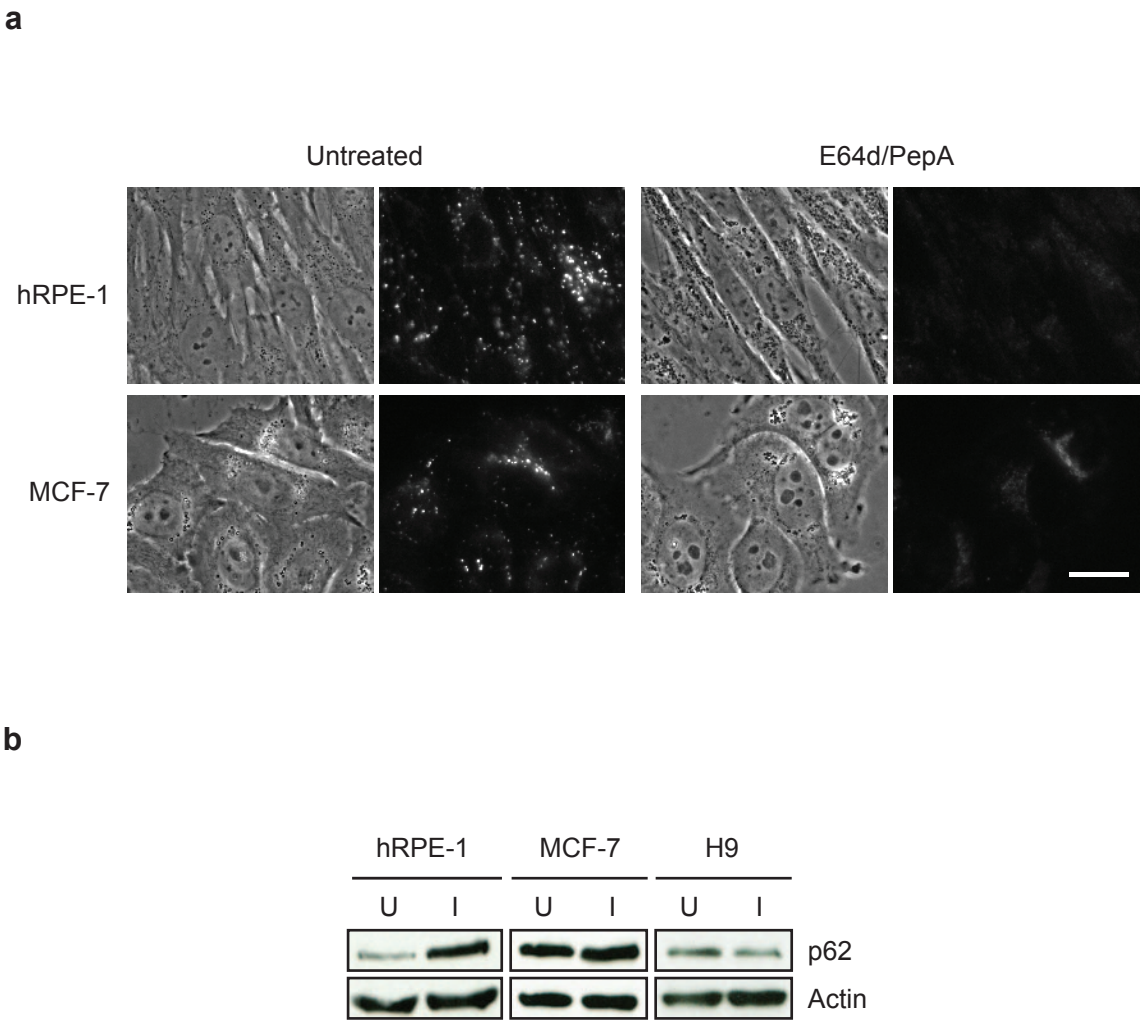

Figure S4 Effects of lysosomal inhibition. (**a**) Lysosomal activity is visualized by fluorescent DQ-BSA. DQ-BSA substrates fluoresce when degraded in lysosomes (left, untreated) but not when lysosomal enzymes are blocked (right panels), confirming function of inhibitors. Bar, 20 μm. (**b**) Use of p62, another protein degraded by autophagy, as an indicator of autophagic flux confirms LC3-II results (Fig. 6d). I, inhibited by lysosomal inhibitors as in Fig. 6d. U, uninhibited. Actin, loading control.

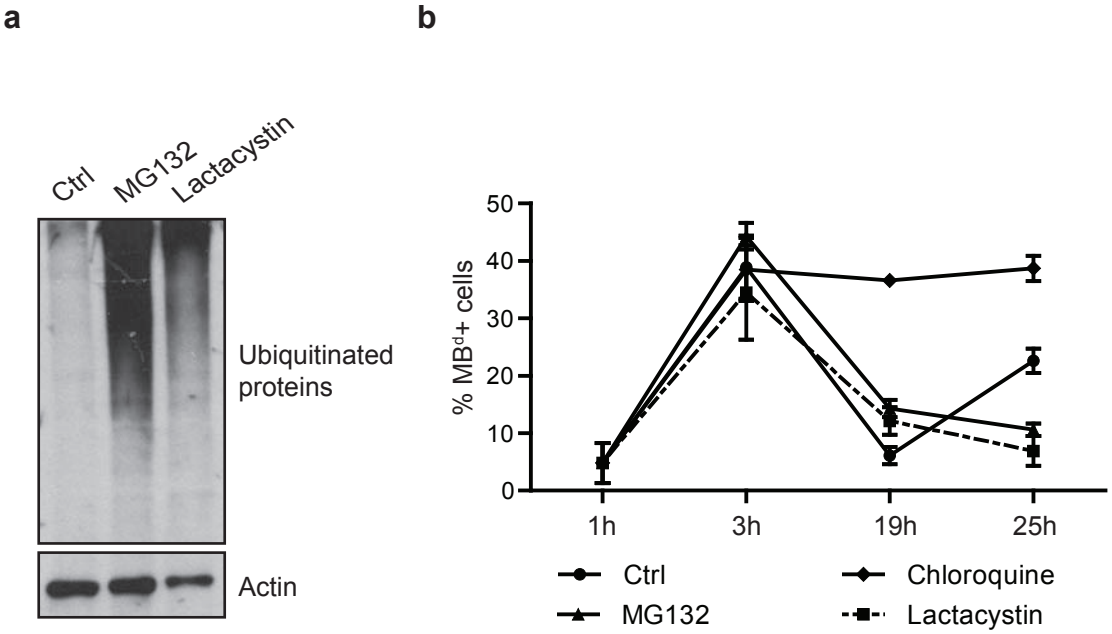

Figure S5 The proteasome does not play a role in MB^d degradation. (**a**) Ubiquitinated protein levels, assessed by anti-ubiquitin antibody, increase in cells treated with proteasome inhibitors (MG132, lactacystin) as indicated, confirming proteasome inhibition. (**b**) Proteasome inhibition has no significant effect on MB^d degradation in hRPE-1 cells compared with the lysosomal inhibitor chloroquine. It only slightly slows the process of MB^d clearance, as control cells have removed most MB^ds by 19 hours. They reenter mitosis and begin to make additional MB^ds from 19-25 hours. Assays were performed by collecting mitotic cells after mitotic shake-off and treating cells with drugs 1 hour after re-plating, when most cells were in cytokinesis. This is to avoid arresting cells in mitosis and thus blocking MB formation. MB^d levels (the percent of MB^d+ cells) are determined as described above.

Fig. 6b

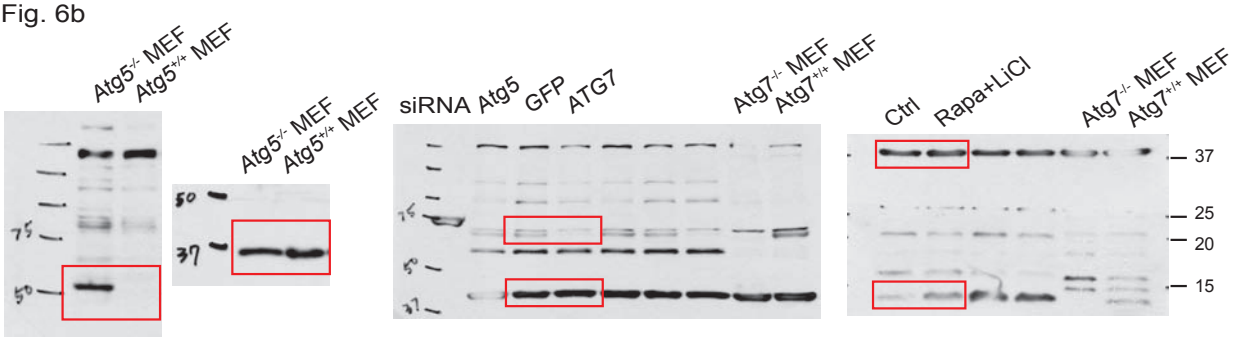

Fig. 6d. All images here are horizontally inversed in main figures.

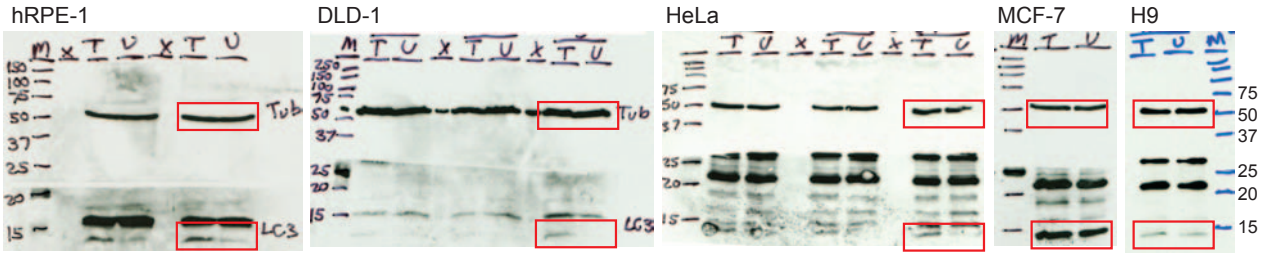

Fig. 7b

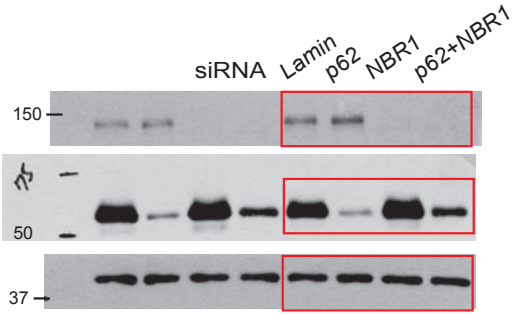

Fig. 7c

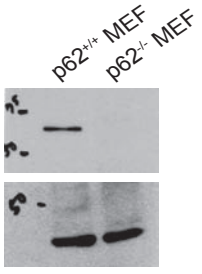

Fig. 7d

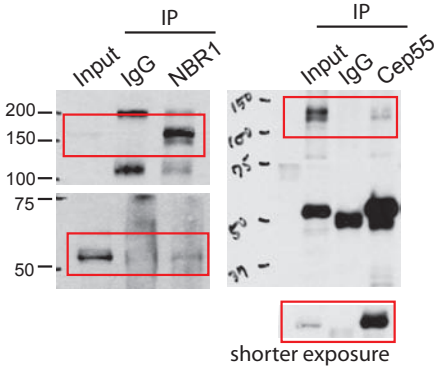

Fig. 8b

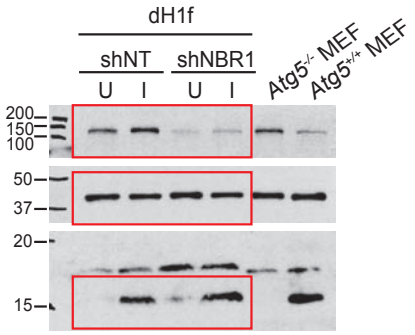

Supplementary Fig. 4b

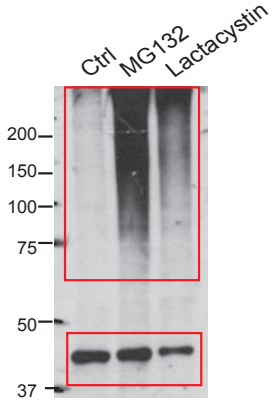

Supplementary Fig. 2d. All images here are horizontally inversed in main figures.

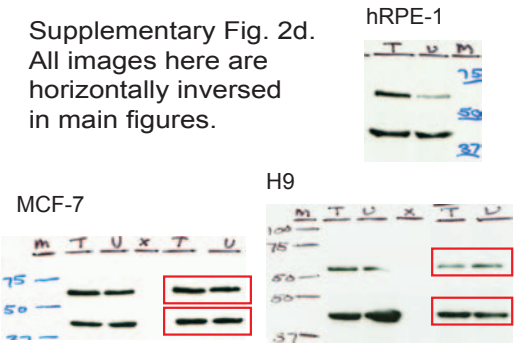

Figure S6 Full scan data of immunoblots. The bands shown in the figures are indicated by the boxed regions.

Supplementary Table 1 Reprogramming is more efficient following an increase in MB^d levels by NBR1 depletion. Fibroblast-like cells differentiated from H1-OGN (dH1f), human embryonic fibroblasts (IMR90), and human adult fibroblasts (hFib2) selected for stable expression of NBR1-specific (shNBR1) or non-targeting shRNA (shNT) are reprogrammed (Fig. 8a, b). The numbers of iPSC colonies in each reprogramming experiment are summarized in the table.

dH1f

experiment	1	2	3	4	5	6	7	8	9
shNT	137	466	250	9	11	20	88	78	120
shNBR1	242	708	703	56	96	91	160	280	210

dH1f-continued

experiment	10	11	12	13	14	5
shNT	21	27	24	39	47	27
shNBR1	71	26	70	84	72	56

IMR90

experiment	1	2	3
shNT	14	49	125
shNBR1	59	199	222

hFib2

experiment	1	2	3	4	5	6
shNT	27	51	28	423	411	501
shNBR1	39	64	69	662	771	656